MUNICH SCHOOL OF ENGINEERING

Professorship of Multiscale Modeling of Fluid Materials

TECHNICAL UNIVERSITY OF MUNICH

Master's Thesis in Materials Science and Engineering

# Directional Solidification of Alloys for Additive Manufacturing

Zhiwei Cao

MUNICH SCHOOL OF ENGINEERING

Professorship of Multiscale Modeling of Fluid Materials

TECHNICAL UNIVERSITY OF MUNICH

Master's Thesis in Materials Science and Engineering

# Directional Solidification of Alloys for Additive Manufacturing

Author: Zhiwei Cao
Supervisor: Prof. Dr. Julija Zavadlav
Submission Date: 10.08.2021

# Acknowledgments

Firstly, my foremost thanks go to my supervisor, Prof. Dr. Julija Zavadlav who has given me numerous important suggestions and invaluable guidance during the period of my thesis writing. Her wonderful topic selection arouses my strong interest in the study of directional solidification and she maintains efficient communication with me to ensure that I can complete the thesis smoothly.

Secondly, my heart-felt thanks also go to all the teachers who have taught me or given me advice on my studies or daily life in my past twenty years' study. The knowledge you taught me is the substantial foundation for my Master's Thesis as well as my future entrepreneurial work and study pursuing higher aspirations.

I would also like to express my sincere thanks to my classmates, also my friends, Fushuai Liu, Maximilian Stupp, Artur Toshev, and Micheal Zartenar. They have provided me a great deal of help and encouragement during my Master's study.

A special thanks to my beloved girlfriend, Yingqiu Lyu. It is your accompany that sees me through the confusion and frustration.

Finally, my deep and sincere gratitude to my family. Only with their selfless support, concern, and love, can I overcome those difficulties and pursue my study till now. Their loving considerations and help are the source of my strength.

# Abstract

Additive manufacturing (AM) is an important and rapidly emerging manufacturing technology nowadays. The heat evolution during AM processes is complex and often limited in small areas, of which directional solidification is an integrated part. Although with a much higher cooling rate and temperature gradient, directional solidification is an integrated part of AM, which is the same as in conventional processes like casting. Therefore, improved understanding of the directional solidification of alloys for AM enables us to discover new alloys appropriate for AM.

Molecular dynamics (MD) has been proved to be reliable in the study of nucleation and solidification. Detailed nanoscale evolution of atoms in the system can be revealed using MD simulation. Simulation of metals using MD was performed in many studies before, while solidification of alloys, especially directional solidification, has not been sufficiently investigated.

Therefore, in this study, MD simulations are performed in order to understand the directional solidification mechanism during AM process. Several alloy systems are investigated from different aspects. The feasibility of simulating AlSi10Mg alloy using existing modified embedded-atom method (MEAM) potentials in MD is discussed. The dependence of temperature for directional solidification simulation is verified on Al - 10% at Mg alloy system. Directional solidification of the 304L stainless steel is successfully simulated using embedded-atom method (EAM) potential by applying a temperature gradient to a fully melted Fe-Cr-Ni system. A directional growth of solid phase from low temperature region towards high temperature region is observed in the simulation box. When fully solidified, the heterogeneity of grains in the final product is studied. To investigate the mechanical properties of the solidified system, uniaxial tensile tests were carried out, in the course of which transformation induced plasticity (TRIP) effect is confirmed because of the occurrence of the phase change ($\gamma \rightarrow \varepsilon \rightarrow \alpha'$) caused by the tensile load. Moreover, a heat shock is applied to the solidified system to inspect the response of the system, which revealed the thermal properties of the system as well. This study can be considered as a preliminary attempt to investigate the topic of directional solidification in AM process.

# Contents

# 1. Introduction

As an integrated phenomenon, rapid directional solidification occurs in various manufacturing processes of metals and alloys, not only in conventional processes like casting, also in contemporary processes like additive manufacturing (AM) [1, 2]. Especially, during the AM, the processed metals and alloys go through a serial of complicated thermal processes [3, 4], which leads to intricate nano- and microstructure of the final product [5, 6, 7, 8].

For example, in the selective laser melting (SLM) process (Fig. 1.1), each layer of metal is created by scanning a laser beam on a designated cross-sectional area of metal powder. Due to the highly concentrated energy and extremely short interaction time, the metal powder scanned by the laser will soon melt and create a melt pool, then the melt pool will solidify at a high cooling rate in the range of about $10^3 - 10^8 K/s$ [8, 9]. As can be seen in Fig.1.1, directional solidification can happen at the interface of the melt pool and neighboring solid. This temperature gradient in the solidification region can be as high as $5 \times 10^6 K/m$ [9].

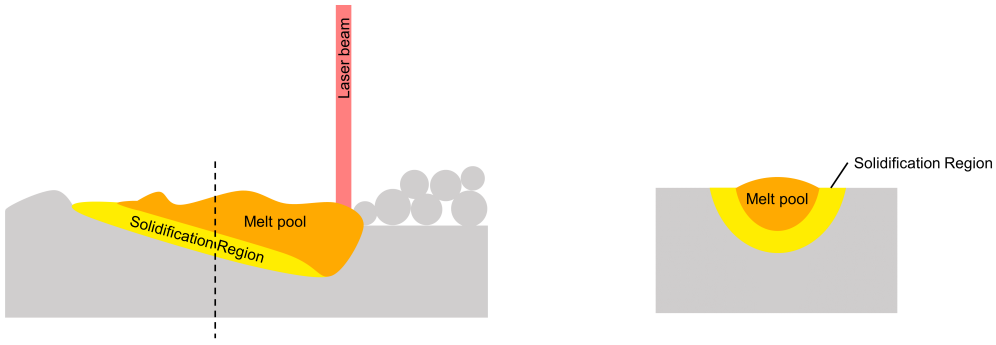


(a) (b)

Figure 1.1.: Schematic illustration of SLM process.(a) cross-sectional view parallel to the moving direction of the laser beam, and (b) cross-sectional view at dashed line position of (a). [10, 11]

Direct observation and investigation of the evolution of the nano- and microstructure during these thermal processes is challenging. Therefore, new methods of investigation in nano- and microscale are required. Computational methods have gained increased popularity in the study of melting and solidification of AM. On macroscale ($> \sim 10^{-3} m$), thermal models, such as computational fluid dynamics and finite element method, can simulate single to multiple melt tracks and layers during AM, but cannot track microstructure evolution like porosity and defects [12, 13, 14]. Models with a length scale between $\sim 10^{-4} - 10^{-2} m$ are called mesoscale models, such as kinetic Monte Carlo [15] and cellular automataton [16, 17], they simulate multiple grains and mainly focus on overall grain structure [18, 19]. Phase-field method, as a microscale ($\sim 10^{-6} - 10^{-4} m$) method, was

frequently applied in the study of dendrite structure formed during solidification [20, 21, 22]. But phase-field method only models the solidification part without the melting part, which means it needs predefined positions of nucleation seeds. This predefined positioning can cause bias, and changing simulation parameters might require new positioning of seeds [14].

Molecular dynamics (MD) is a simulation method using Newton's equation of motion to analyze the physical movements of atoms and molecules [23, 24]. MD simulation shows its reliability in the study of nucleation and solidification, and successfully reveals the heterogeneity of homogeneous nucleation of pure iron [25]. For AM process, researchers have performed numerous studies to simulate and investigate materials evolution on nanoscale [26, 27, 28]. Directional solidification is what happens in the real-world AM process, as the conditions of homogeneous solidification are hard to reach. However, the MD studies focused on rapid directional solidification on nanoscale during AM process are rare. Mahata et al. [29] investigated the rapid directional solidification of Al-Cu alloys using modified embedded-atom method (MEAM) potential and discussed the effect of mechanical properties on the final product. Bahramyan et al. [30] studied the rapid directional solidification of Fe-Cr-Ni alloys using a large-scale MD simulation with 15M atoms and investigated the mechanical properties and defects. Besides the study of Bahramyan et al., no other study of the directional solidification of stainless steel during AM process has been reported.

AlSi10Mg is one of the most commonly used Al alloys for AM. 304L stainless steel, which can also be used in AM, is well-known for its application in both households and industries. The materials processed in AM experience a rapid heating and cooling rate, which can lead to products with microstructure very different form conventionally processed ones. For example, the existence of the dislocation network in products manufactured by SLM is reported to significantly improve the strength and ductility of stainless steel [31]. Anisotropy of tensile properties in different directions of metallic AM samples has been reported [32, 33]. What's more, in the process of SLM, when the high-energy laser continuously scans through the whole designated section, it can be very close to the previous melting pool where the melting and solidification process has already finished, which results in another significant temperature rise in this region [7]. In this study, this abrupt reheating is simulated as a thermal shock. Currently, there are studies on thermal shock on W [34] and Cu [35] using MD.

One important behavior of 304L stainless steel is the so-called transformation induced plasticity (TRIP) effect. The 304L stainless steel is an austenitic stainless steel with a low stacking-fault-energy face-centered cubic (FCC) structure. Plenty of studies [36, 37, 38] have shown that martensitic transformation can occur in this metastable austenitic stainless steel upon deformation, which is because of the so-called TRIP effect. This transformation can lead to a good strength and ductility combination. The sequence for this martensitic transformation is $\gamma \rightarrow \varepsilon \rightarrow \alpha'$, which are FCC, HCP, and BCC structure, respectively [39, 40].

In this study, theoretical basics of solidification and MD simulation using EAM or MEAM potential are discussed in Chapter 2. In Chapter 3, the possibility of using MEAM potential to simulate the behavior of AlSi10Mg alloys during the directional solidification process is verified, followed by the determination of optimal temperature setup for simulating Al-10 at % Mg alloy in directional solidification. Rapid directional solidification of SAE 304L stainless steel was performed utilizing EAM potential. Afterward, a comprehensive study of this simulation focusing on nanostructure, mechanical and thermal properties is conducted, which also gives a preliminary approach on further study of directional solidification of other alloys.

# 2. Methods

## 2.1. Molecular Dynamics

Molecular Dynamics (MD) is a simulation method for computing the time evolution of a classical many-body molecular or atomic system. Here, "classical" means that the motion of atoms or molecules obeys the laws of classical mechanics (Newton's laws of motion), which is an excellent approximation for a wide range of materials under most circumstances [24].

The basic procedure of molecular dynamic simulation contains the following steps: (i) input parameters to specify the conditions of the simulation (e.g., timestep, interatomic potential, etc.); (ii) initialization of the system (i.e., initial positions and velocities); (iii) calculation of the interatomic forces for every atom, (iv) update of the velocity and position of every atom according to Newton's laws of motion. Step (iii) and (iv) are repeated until the desired simulation time is reached. Macroscopic observables such as pressure, energy, and heat capacity, etc. can be inferred from microscopic information of positions and velocities of atoms using statistical mechanics.

### 2.1.1. Newton's Equation of Motion

According to Newton's second law, for every particle in a MD system,

$$\boldsymbol{F}_i(t) = m_i \boldsymbol{a} = m_i \frac{\mathrm{d}^2 \boldsymbol{r}_i(t)}{\mathrm{d}t^2}, \tag{2.1}$$

where $F_i(t)$ is the force on particle $i$ at time $t$, $m_i$ is the mass of the particle, $r_i(t)$ is the coordinate of the particle at time $t$.

$F_i(t)$ can be determined by interatomic potential $E$

$$\boldsymbol{F_i} = -\frac{\partial}{\partial \boldsymbol{r}_i} E_i, \tag{2.2}$$

By solving Eqn. 2.1 and Eqn. 2.2, the forces of all particles in the simulation system can be obtained. Then the corresponding position, velocity, and other motion information can be calculated. Furthermore, the positions and velocities of all particles in the system at any time can be attained.

### 2.1.2. Integration Algorithm

To determine the positions and velocities of a particle using Eqn. 2.1, an integration algorithm is needed. The commonly used integration algorithms for MD are Verlet algorithm [41], velocity Verlet algorithm [42], leapfrog algorithm [43], etc.

#### 2.1.2.1. Verlet Algorithm

Based on the finite difference method, the Verlet algorithm divides the total time of particle movement into a finite number of segments, with timestep as the length of the segment.

Then the forward Taylor expansion and backward Taylor expansion can be written as Eqn. 2.3 and Eqn. 2.4:

$$\boldsymbol{r}(t+\Delta t) = \boldsymbol{r}(t) + \boldsymbol{v}(t)\Delta t + \frac{1}{2}\boldsymbol{a}(t)\Delta t^2 + \frac{1}{3!}\boldsymbol{b}(t)\Delta t^3 + O\left(\Delta t^4\right), \tag{2.3}$$

$$\boldsymbol{r}(t-\Delta t) = \boldsymbol{r}(t) - \boldsymbol{v}(t)\Delta t + \frac{1}{2}\boldsymbol{a}(t)\Delta t^2 - \frac{1}{3!}\boldsymbol{b}(t)\Delta t^3 + O\left(\Delta t^4\right), \tag{2.4}$$

where $\boldsymbol{a}(t)$ is the acceleration at time $t$, $\boldsymbol{b}(t)$ is the third derivative of particle position $\boldsymbol{r}$ at time $t$. Combining Eqn. 2.3 and Eqn. 2.4, we obtain

$$\boldsymbol{r}(t+\Delta t) = 2\boldsymbol{r}(t) - \boldsymbol{r}(t-\Delta t) + \boldsymbol{a}(t)\Delta t^2 + O\left(\Delta t^4\right). \tag{2.5}$$

Eqn. 2.5 is the basic form of Verlet algorithm. New position can be directly calculated without knowing velocity. However, if velocity is needed (e.g., for the determination of system temperature), it can be derived by subtracting Eqn. 2.3 and Eqn. 2.4, i.e.,

$$\boldsymbol{r}(t+\Delta t) - \boldsymbol{r}(t-\Delta t) = 2\boldsymbol{v}(t)\Delta t + O\left(\Delta t^2\right), \tag{2.6}$$

$$\Rightarrow \boldsymbol{v}(t) = \frac{\boldsymbol{r}(t+\Delta t) - \boldsymbol{r}(t-\Delta t)}{2\Delta t} + O\left(\Delta t^2\right). \tag{2.7}$$

It can be seen that the velocity calculated via the Verlet algorithm is less accurate than the position.

#### 2.1.2.2. Velocity Verlet Algorithm

With velocity explicitly incorporated, velocity Verlet algorithm improved by Swope [42] is a more commonly used integration method in MD simulations. The standard implementation procedure of this algorithm is:

1. Initialization with setup of the system at time $t$.
2. Calculation of new position at time $(t+\Delta t)$

$$\boldsymbol{r}(t+\Delta t) = \boldsymbol{r}(t) + \boldsymbol{v}(t)\Delta t + \frac{1}{2}\boldsymbol{a}(t)\Delta t^2. \tag{2.8}$$

3. Calculation of the intermediate velocity at $(t+\frac{1}{2}\Delta t)$

$$\boldsymbol{v}(t+\frac{1}{2}\Delta t) = \boldsymbol{v}(t) + \frac{1}{2}\boldsymbol{a}(t)\Delta t. \tag{2.9}$$

4. Calculation of new acceleration $\boldsymbol{a}(t+\Delta t)$ with the new position $\boldsymbol{r}(t+\Delta t)$.
5. Calculation of new velocity $\boldsymbol{v}(t+\Delta t)$

$$\begin{aligned}\boldsymbol{v}(t+\Delta t) &= \boldsymbol{v}(t+\frac{1}{2}\Delta t) + \frac{1}{2}\boldsymbol{a}(t+\Delta t)\Delta t \\ &= \boldsymbol{v}(t) + \frac{1}{2}\boldsymbol{a}(t)\Delta t + \frac{1}{2}\boldsymbol{a}(t+\Delta t)\Delta t.\end{aligned} \tag{2.10}$$

Then the velocity Verlet algorithm can be expressed as:

$$\boldsymbol{r}(t+\Delta t) = \boldsymbol{r}(t) + \boldsymbol{v}(t)\Delta t + \frac{1}{2}\boldsymbol{a}(t)\Delta t^2. \tag{2.11}$$

$$\boldsymbol{v}(t+\Delta t) = \boldsymbol{v}(t) + \frac{\boldsymbol{a}(t) + \boldsymbol{a}(t+\Delta t)}{2}\Delta t. \tag{2.12}$$

With this algorithm, the position, velocity, and acceleration of each particle can be derived simultaneously without losing accuracy.

### 2.1.3. Force Fields

The interatomic potential is the fundamental factor of the reliability and accuracy of the simulation results. Based on Eqn. 2.2, to run an MD simulation, the force on each particle which is also defined by the gradient of the potential energy function needs to be defined.

#### 2.1.3.1. Embedded Atom Method (EAM)

In 1983, Daw and Baskes [44] proposed the embedded-atom method (EAM) based on density functional theory, as a new approach of calculating properties of metal systems. According to EAM, all atoms in the system are considered as "impurity" being embedded in the host consisting of all other atoms. When calculating the total energy of the system, the energy is divided into two parts, one is the embedding energy to embed atoms into the electron cloud, the other part is the pair potential between two atoms. The energy of atom $i$ in EAM is given by

$$E_{tot} = \sum_i F_i(\rho_i) + \frac{1}{2} \sum_{\substack{i,j \\ i \neq j}} \phi_{ij}(R_{ij}), \tag{2.13}$$

where $F_i$ is the embedding potential energy of atom $i$, which is a function of the electron density $\rho_i$ only; $\phi_{ij}$ is the short-range pair potential, and $R_{ij}$ is the distance between atoms $i$ and $j$. The electron density $\rho_i$ is a linear summation of electron cloud density of all atoms in the system except atom $i$, and can be expressed as

$$\rho_i = \sum_{\substack{j \\ j \neq i}} \rho_j^a(R_{ij}). \tag{2.14}$$

Here $\rho_j^a$ is the contribution to the density from atom $j$.

This classical EAM expression has been successfully applied to the FCC [44], BCC [45], and nearly filled d-band transition metals [46].

#### 2.1.3.2. Modified Embedded Atom Method (MEAM)

To extend the application of the EAM potential to more types of atoms, Baskes, etc. made some modifications to the classical EAM [47, 48], which enabled the modeling of silicon and germanium. A more general modified embedded-atom method (MEAM), which covers metals, semiconductors, and diatomic gaseous elements, was proposed in 1992 by Baskes [49]. With MEAM, the simplification of first-neighbor interactions for all crystal structures (including BCC, HCP, and diamond cubic) was made possible.

Similar to Eqn. 2.13 of EAM, the total energy of a system in MEAM is approximated as

$$E_{tot} = \sum_i F_i(\overline{\rho}_i) + \frac{1}{2} \sum_{\substack{i,j \\ i \neq j}} \phi_{ij}(R_{ij}), \tag{2.15}$$

where the difference is the $\overline{\rho}_i$, which is the electron densities modified by angular-dependent terms instead of the linear approximation of spherically averaged electron densities $\rho_i$ in EAM.

The embedding function $F(\overline{\rho})$ can be expressed as

$$F(\overline{\rho}) = AE_c\overline{\rho}_i \ln \overline{\rho}_i, \tag{2.16}$$

where $A$ is an adjustable parameter, $E_c$ is the sublimation energy, $\overline{\rho}_i$ is the background electron density, which is composed of spherically symmetric partial electron density $\overline{\rho}_i^{(0)}$ and angular contributions $\overline{\rho}_i^{(1)}$, $\overline{\rho}_i^{(2)}$, $\overline{\rho}_i^{(3)}$ (definition in Eqn. 2.21). $\overline{\rho}_i$ is given by

$$\overline{\rho}_i = \frac{\overline{\rho}_i^{(0)}}{\rho_i^0} G_i(\Gamma_i), \tag{2.17}$$

where $G_i(\Gamma)$ is a function that can be different for different element types in a simulation system. Common choices for $G(\Gamma)$ can be $G(\Gamma) = \sqrt{1+\Gamma}$, $G(\Gamma) = exp(\Gamma/2)$, $G(\Gamma) = 2/(1+exp(-\Gamma))$, etc [50]. And $\Gamma_i$ is given by

$$\Gamma_i = \sum_{k=1}^{3} t_i^{(k)} \left( \frac{\overline{\rho}_i^{(k)}}{\overline{\rho}_i^{(0)}} \right)^2, \tag{2.18}$$

where the average weighting factors $t_i^{(k)}$ will be discussed in Eqn. 2.23.

The composition-dependent electron density scaling $\rho_i^0$, or the background electron density for a reference structure, is defined as

$$\rho_i^0 = \rho_{i0} Z_{i0} G(\Gamma_i^{ref}), \tag{2.19}$$

where $\rho_{i0}$ is an element-dependent density scaling, $Z_{i0}$ is the first-neighbor coordination of the reference system.

$\Gamma_i^{ref}$ is given by

$$\Gamma_i^{ref} = \sum_{k=1}^{3} t_i^{(k)} \frac{s_i^{(k)}}{Z_{i0}^2}, \tag{2.20}$$

where $s_i^{(k)}$ are shape factors determined by the reference structure for atom $i$ [49].

The partial electron densities $\overline{\rho}_i^{(0)}$, $\overline{\rho}_i^{(1)}$, $\overline{\rho}_i^{(2)}$, and $\overline{\rho}_i^{(3)}$ are given by

$$\left(\overline{\rho}_i^{(0)}\right)^2 = \left[ \sum_{j \neq i} \rho_j^{a(0)} \left(R_{ij}\right) S_{ij} \right]^2, \tag{2.21a}$$

$$\left(\overline{\rho}_i^{(1)}\right)^2 = \sum_{\alpha=1}^{3} \left[ \sum_{j \neq i} \rho_j^{a(1)} \frac{R_{ij\alpha}}{R_{ij}} S_{ij} \right]^2, \tag{2.21b}$$

$$\left(\overline{\rho}_i^{(2)}\right)^2 = \sum_{\alpha=1}^{3} \sum_{\beta=1}^{3} \left[ \sum_{j \neq i} \rho_j^{a(2)} \frac{R_{ij\alpha} R_{ij\beta}}{R_{ij}^2} S_{ij} \right]^2 - \frac{1}{3} \left[ \sum_{j \neq i} \rho_j^{a(2)} \left(R_{ij}\right) S_{ij} \right]^2, \tag{2.21c}$$

$$\left(\overline{\rho}_i^{(3)}\right)^2 = \sum_{\alpha=1}^{3} \sum_{\beta=1}^{3} \sum_{\gamma=1}^{3} \left[ \sum_{j \neq i} \rho_j^{a(3)} \frac{R_{ij\alpha} R_{ij\beta} R_{ij\gamma}}{R_{ij}^3} S_{ij} \right]^2 - \frac{3}{5} \sum_{\alpha=1}^{3} \left[ \sum_{j \neq i} \rho_j^{a(3)} \frac{R_{ij\alpha}}{R_{ij}} S_{ij} \right]^2, \tag{2.21d}$$

where $R_{ij}^{\alpha}$ is the $\alpha$ component of the distance vector between atoms $i$ and $j$. $\rho_i^{a(k)}$, representing the atomic electron densities from $j$ atom at distance $R_{ij}$ from position $i$, are computed as

$$\rho_i^{a(k)}\left(R_{ij}\right) = \rho_{i0} \exp\left[-\beta_i^{(k)}\left(\frac{R_{ij}}{r_e} - 1\right)\right], \tag{2.22}$$

where $r_e$ is the nearest-neighbor distance in the equilibrium single-element reference structure, $\beta_i^{(k)}$ are adjustable parameters depending on elements.

The average weighting factors $t_i^{(k)}$ in Eqn. 2.18 and Eqn. 2.20 are given by

$$t_i^{(k)} = \frac{1}{\bar{\rho}_i^{(0)}} \sum_{j \neq i} t_{0,j}^{(k)} \rho_j^{a(0)} S_{ij}, \tag{2.23}$$

where $t_{0,j}^{(k)}$ are adjustable parameters.

$S_{ij}$ in Eqn. 2.21 and Eqn. 2.23 is the many-body screening function between atoms $i$ and $j$, which ranges from 1 (unscreened) to 0 (completely screened or outside the cutoff radius). $S_{ij}$ is defined as

$$S_{ij} = \overline{S}_{ij} f_c(\frac{r_c - R_{ij}}{\Delta r}), \tag{2.24}$$

where

$$\overline{S}_{ij} = \prod_{k \neq i,j} S_{ikj}, \tag{2.25}$$

and $r_c$ is the cutoff radius, $\Delta r$ is the length of smoothing distance for cutoff function, $S_{ikj}$ is the screening factor, and $k$ represents all other neighbor atoms. To determine $S_{ikj}$, an ellipse passing through atom $i$, $j$, and $k$, with $i$ and $j$ on the major axis, is constructed on an x-y plane (Fig. 2.1). So the equation of the ellipse can be expressed as

$$x^2 + \frac{1}{C} y^2 = (\frac{1}{2} R_{ij})^2, \tag{2.26}$$

where $C$ is determined by

$$C = \frac{2(X_{ik} + X_{kj}) - (X_{ik} - X_{kj})^2 - 1}{1 - (X_{ik} - X_{kj})^2}, \tag{2.27}$$

where $X_{ik} = (R_{ik}/R_{ij})^2$ and $X_{kj} = (R_{kj}/R_{ij})^2$. The screening factor $S_{ikj}$ is a function of $C$ as follows

$$S_{ikj} = f_c\left(\frac{C - C_{min}}{C_{max} - C_{min}}\right), \tag{2.28}$$

where the smooth cutoff function $f_c$ is defined as

$$f_c = \begin{cases} 0 & x \leq 0 \\ [1 - (1-x)^4]^2 & 0 < x < 1 \\ 1 & x \geq 1, \end{cases} \tag{2.29}$$

$C_{min}$ and $C_{max}$ are the limiting values of $C$ determining the extent of screening. $C_{min}$ and $C_{max}$ are defined separately for each $i - j - k$ triplet, based on there element types. In original MEAM, $C_{min} = 2.0$ and $C_{max} = 2.8$ were chosen [49].

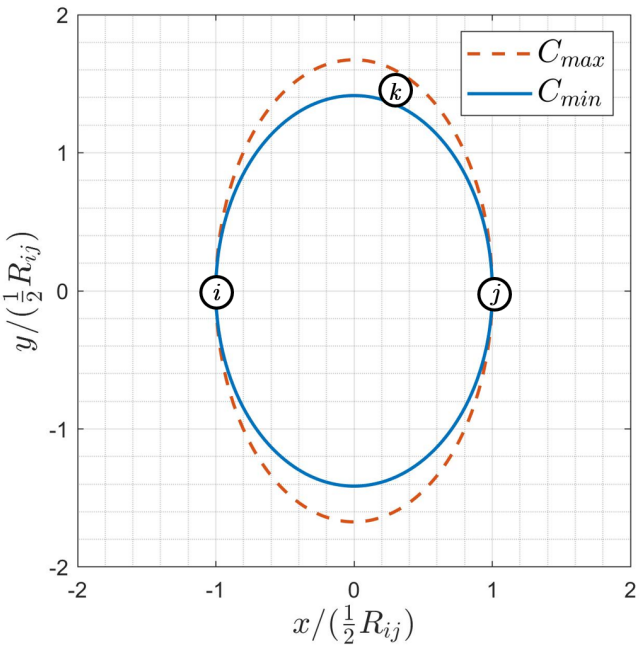


Figure 2.1.: Screening of atoms $i$ and $j$ by neighboring atom $k$. Atoms outside $C_{max} = 2.8$ do not have any effect on the interaction between atoms $i$ and $j$; atoms inside $C_{min} = 2.0$ completely screen atoms $i$ and $j$ ; atoms in between $C_{min}$ and $C_{max}$ screen partially according to Eqn. 2.28.

In MEAM, there is no specific functional expression given directly to pair potential $\phi(R)$. It is computed from known values of the total energy and the embedding energy [51]. According to Eqn. 2.15, the energy per atom for reference structure $E^u(R)$ in MEAM can be expressed as a function of the first nearest-neighbor distance $R$

$$E^u(R) = F\left[\rho^0(R)\right] + \frac{1}{2}\sum \phi(R), \tag{2.30}$$

where $\rho^0$ is defined in Eqn. 2.19.

#### 2.1.3.3. Second Nearest-Neighbor Modified Embedded Atom Method (2NN MEAM)

The first nearest-neighbor MEAM discussed above is applicable for a wide range of elements and alloys. However, it doesn't reproduce the properties of BCC metals very satisfyingly [52]. Because the second nearest-neighbor distance is only 15% larger than the first nearest-neighbor distance in BCC structure, the interaction with the second nearest-neighbor atoms may not be negligible. So Lee and Baskes proposed second nearest-neighbor modified embedded-atom method (2NN MEAM) in 2000 [52], which took the interactions of second nearest-neighbors into consideration.

Firstly, the screening is too strict for BCC structure. The many-body screening function should be adjusted to a less strong degree. This can be achieved by assigning a value lower than 2.0 and 1.0 to $C_{min}$ for BCC and FCC metals respectively. For example, for BCC metal V, $C_{min} = 0.49$ is chosen [53].

Secondly, pair potential $\phi(R)$ should also include the interaction of the second nearest-neighbor. The energy per atom in a reference structure $E^u(R)$ should also take the second

nearest-neighbor into account, which can be expressed as an extension of Eqn. 2.30

$$E^u(R) = F\left[\rho^0(R)\right] + \frac{Z_1}{2}\phi(R) + \frac{Z_2 S}{2}\phi(aR), \tag{2.31}$$

where $Z_2$ is the number of second nearest-neighbor atoms, $a$ is the ratio of the distance of the second nearest-neighbor and the first nearest-neighbor, the background electron density $\rho^0$ taking the second nearest-neighbor into account

$$\rho^0(R) = Z_1\rho^{a(0)}(R) + Z_2 S\rho^{a(0)}(aR). \tag{2.32}$$

### 2.1.4. Temperature and Pressure Control

The concept of statistical ensemble was proposed by Gibbs [54] in the analysis of thermodynamic systems using statistical mechanics. It refers to a collection of numerous (sometimes infinite) virtual duplicates of a certain system, each of which represents a possible state that the real system might be in. In MD simulation, the macro environment of the simulation system needs to be constrained to make the simulation environment close to the real experimental process. To achieve this, the velocities and positions of the particles generated and updated in MD are sampled from several specific ensembles. The thermodynamics ensembles used in this study are:

1. Microcanonical ensemble: isolated thermal equilibrium states of a system with no exchange of energy or particles with its environment. The total number of particles in the system ($N$), the volume of the system ($V$), and the total energy ($E$) of the system are constant. Also called NVE ensemble.

2. Canonical ensemble: thermal equilibrium states of a system kept in a fixed temperature "heat bath". The total number of particles in the system ($N$), the volume of the system ($V$), and the system temperature ($T$) of the system are constant. Also called NVT ensemble.

3. Isothermal-isobaric ensemble: thermal equilibrium states of a system with constant pressure ($P$) and constant temperature ($T$). Also called NPT ensemble.

In this study, several different temperature and pressure control methods are applied in order to guarantee the ensemble of the system, thus regulating various simulation situations. These methods are called thermostat and barostat respectively, for example, Nose-Hoover thermostat using non-Hamiltonian equations of motion [55], Langevin thermostat [56], and Parrinello-Rahman barostat [57].

### 2.1.5. Software

In this study, Large-scale Atomic/Molecular Massively Parallel Simulator (LAMMPS) [58] is chosen to perform all simulations. LAMMPS, designed for efficient parallel computing, is an open-source molecular dynamics simulation software developed originally at Sandia National Laboratories.

Atomsk [59] is adopted in this work for constructing initial atomic-scale models of simulations, as it offers easy-to-use options for elementary transformations on atomic models.

OVITO [60] and Python codes are used for the post-process and visualization of LAMMPS output data.

## 2.2. Solidification

### 2.2.1. Solidification Theory

For a metallic liquid-solid system, the solidification of metallic crystals usually takes place by two processes: nucleation and growth [1].

According to the second law of thermodynamics, at a constant temperature and pressure, the system evolves towards a state with lower system free energy [61]. The Gibbs free energy $G$ can be expressed as

$$G = H - TS, \tag{2.33}$$

where $H$ is enthalpy, $T$ is thermodynamic temperature, and $S$ is entropy. The free energy change with temperature of solid and liquid phase is shown in Fig. 2.2. The melting point $T_m$ is defined as the temperature where the solid and liquid free energy curves intersect.

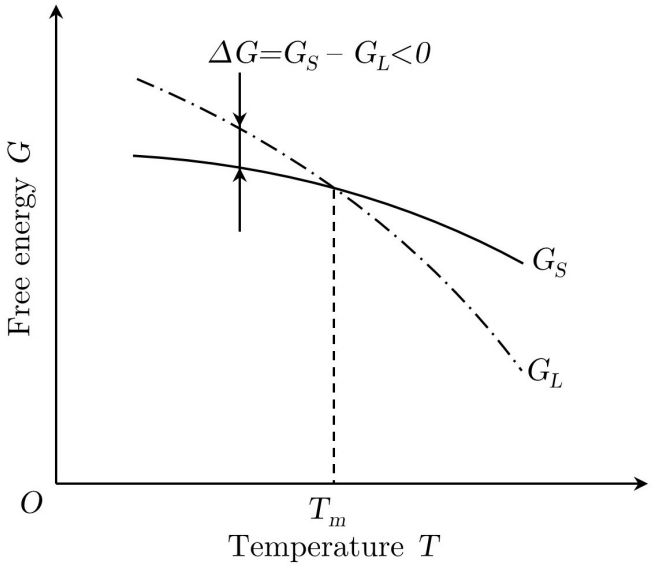


Figure 2.2.: Free energy changes with temperature.

The free energy change of unit volume from the liquid phase to the solid phase is $\Delta G_V$

$$\Delta G_V = G_S - G_L, \tag{2.34}$$

where $G_S$ and $G_L$ are free energy of unit volume of solid and liquid phase, respectively. This equation can be also written as

$$\Delta G_V = \frac{-L_m \Delta T}{T_m}, \tag{2.35}$$

where $L_m$ is the enthalpy of fusion, which means the system absorbs heat from the environment during phase transfer from solid to liquid and is defined to be positive. $\Delta T$ is supercooling degree and is defined as the temperature difference between $T_m$ and actual freezing temperature $T$ ($\Delta T = T_m - T$). It can be inferred from Eqn. 2.35 that the actual freezing temperature should be lower than $T_m$, which means supercooling is necessary.

When the temperature is below the melting point, atom embryos with short-range order can result from a concentration fluctuation of atoms in the liquid phase. These embryos have the possibility of continuing to grow above critical size to form nuclei, because this procedure lowers the system's free energy ($\Delta G_V < 0$). This kind of nucleation is called homogeneous nucleation. Assuming that the nucleus is a sphere with radius $r$, when a nucleus appears in the liquid phase, the total free energy change can be described as two parts, increase of surface energy caused by the formation of the new surface ($4\pi r^2\sigma$) and decrease of volume energy caused by the formation of the new low-energy volume ($\frac{4}{3}\pi r^3 \Delta G_V$). Therefore, the change of total free energy when a nucleus is formed in a supercooled liquid is

$$\Delta G = \frac{4}{3}\pi r^3 \Delta G_V + 4\pi r^2 \sigma, \tag{2.36}$$

where $\sigma$ is surface energy (expressed by surface tension). At constant temperature, $\Delta G_V$ and $\sigma$ are constant, so $\Delta G$ is the function of $r$ (Fig. 2.3). When $r < r^*$, the growth of embryos will cause an increase of system free energy, so embryos of this size are hard to grow and will eventually disappear. When $r \geqslant r^*$, the growth of embryos will reduce free energy, and these embryos will finally become stable nuclei.

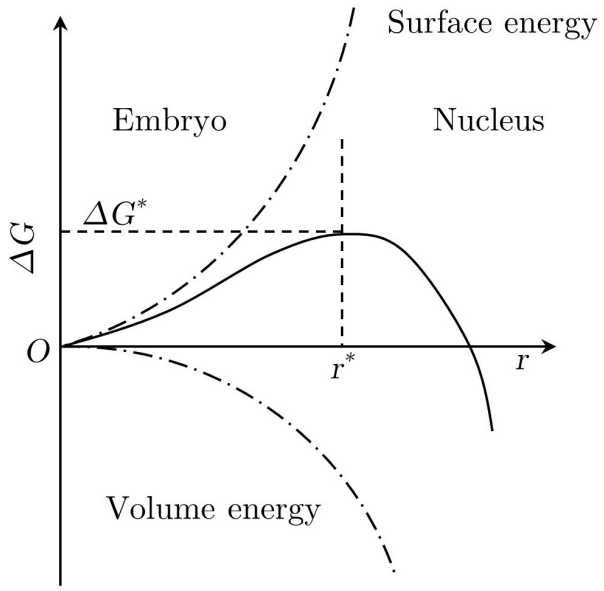


Figure 2.3.: $\Delta G$ changes with $r$ at a constant temperature.

The rate of nucleation $N$ is the number of nuclei formed in unit volume and unit time. It is controlled by two factors, which are related to free energy change during nucleation and atoms diffusion across phase boundary. Therefore nucleation rate can be expressed as

$$N = Kexp(\frac{-\Delta G^*}{k_B T}) \cdot exp(\frac{-Q}{k_B T}), \tag{2.37}$$

where $K$ is constant, $\Delta G^*$ is the change of free energy associated with the formation of a critical nucleus, $Q$ is the energy of activation for diffusion across the phase boundary, $k_B$ is the Boltzmann constant. When supercooling is low, the nucleation rate will increase with

the increase of supercooling because of the decrease of the critical nucleation radius; but if the supercooling increases continuously, the nucleation rate will decrease, because the diffusion of atoms is limited by low temperature. Therefore, there exists a critical degree of supercooling for the highest nucleation rate, for most metals, this critical supercooling is about $0.15 - 0.20\ T_m$ [61].

### 2.2.2. Determination of Melting Point

Melting point is one of the important properties of materials, which is also very important for temperature setup of thermostats in directional solidification simulation.

It is not uncommon for a literature potential to give an accurate prediction of static properties of a certain phase, while in the meantime give numerically unstable simulation results in MD simulation [62]. Therefore, the verification of the melting point of each atomic model is necessary before further studies.

In this study, several potentials were compared to find out which one is the most suitable potential to describe the behavior of AlSi10Mg alloy during the melting and solidification process. The potential used for the simulation of 304L stainless steel was also investigated. In this work, two methods are applied to determine the melting point of simulation systems, namely the hysteresis method and the coexistence method.

#### 2.2.2.1. Hysteresis Method

A straightforward way of determining the melting temperature is gradually and linearly increasing the temperature of the system with perfect lattice configuration. The melting temperature will be the temperature where the sudden change of system properties (density, volume, kinetic energy, etc.) happens, which means the breakdown of the lattice. However, the sudden-change temperature acquired in this way significantly overestimates the actual melting temperature because of superheating [63, 64]. Similarly, when cooling down of a liquid system, supercooling will lead to an underestimate of melting temperature (Fig. 2.4).

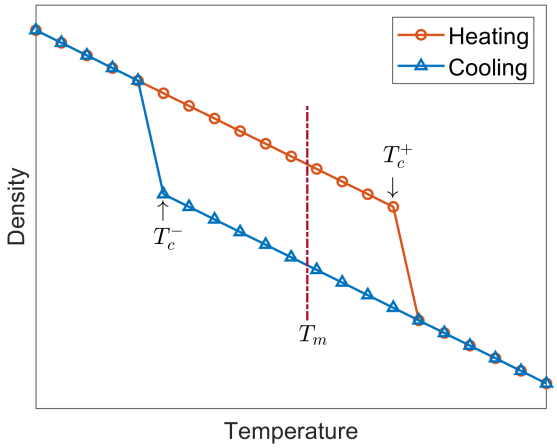


Figure 2.4.: Simplified illustration of typical single-phase melting and refreezing behavior of metal at constant pressure, where the $T_c^+$ is the superheating temperature, $T_c^-$ is the supercooling temperature, and $T_m$ is the equilibrium melting temperature.

This phenomenon of overestimation (or underestimation) of melting temperature caused by superheating (or supercooling) is also called the hysteresis phenomenon. The free energy barrier $\beta$ in the process of melting and solidification leads to this hysteresis phenomenon. According to the theory of homogeneous nucleation melting [65], the free energy barrier $\beta$ depends on the material and can be expressed as

$$\beta = \frac{16\pi\gamma_{sl}^3}{3k_B T_m \Delta H_m^2}, \tag{2.38}$$

where $\gamma_{sl}^3$ is the solid-liquid interfacial energy, $k_B$ is the Boltzmann constant, and $\Delta H_m$ is the heat of fusion. Furthermore, the systematic expression of maximum superheating and supercooling is given phenomenologically

$$\beta = (A_0 - b\log_{10} Q)\theta_c(1-\theta_c)^2, \tag{2.39}$$

where $A_0 = 59.4$, $b = 2.33$, $Q$ is the heating (or cooling) rate normalized by $1K/s$, and $\theta_c$ is the maximum superheating (or supercooling) where $\theta_c = T_c/T_m$, the $T_c$ here is the highest (or lowest) temperature achievable in a superheated (or supercooled) solid. Based on Eqn. 2.39, Luo et al. [66] proposed the hysteresis method, through which the equilibrium temperature at a certain pressure can be calculated directly from the maximum superheating and supercooling:

$$T_m = T_c^+ + T_c^- - \sqrt{T_c^+ T_c^-}. \tag{2.40}$$

This method has been proved to be a conceptually simple and computationally inexpensive way to estimate the equilibrium melting point of metals [67], organic compounds [64], etc.

#### 2.2.2.2. Coexistence Method

The coexistence method requires simulating the liquid-solid coexistence system directly with an explicit interface. This idea had been used in the 1970s but was limited by insufficient computer performance [68, 69, 70]. In 2002 this idea was extended to a larger scale by Morris and Song, in order to calculate the equilibrium melting curve [71]. This coexistence simulation was considered as an alternative to traditional Gibbs free energy calculations.

The first step of this procedure is to create a simulation box containing both liquid and solid phases of the target element or alloy. In this work, the initial simulation boxes containing both liquid and solid phases are created using Atomsk, avoiding problems causing by combining different simulation boxes containing liquid and solid parts together. Pressure in the simulation box caused by thermal expansion is a challenge when performing coexistence method, which will cause bias or even blow up of simulation box. Zhu et al. [72] proposed a solution to relieve this stress by applying a strain to the simulation box. Here in this study, another possible way is proposed, which was adding an empty space in the middle of the liquid phase before melting. This predefined space can contain thermal expansion, thus avoiding stress.

As shown in Fig. 2.5(a), the middle part of the simulation box is assigned as the liquid part, and both ends are assigned as solid parts in order to constrain the thermal expansion of the liquid part. The interfaces between the liquid and solid parts are assigned as y-z planar. Space is created in the middle of the liquid part to adapt to the thermal expansion by shifting half of the atoms along the direction perpendicular to the liquid-solid interface (x-direction). This shifting distance is determined by the ratio of the density of the liquid

and solid (see Table 3.3). Then the solid and liquid parts are relaxed near melting point to create a solid-liquid coexistence state.

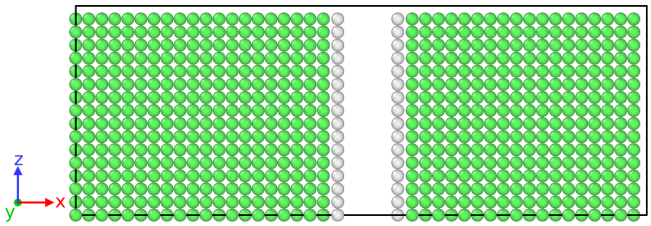


(a) Initial simulation box

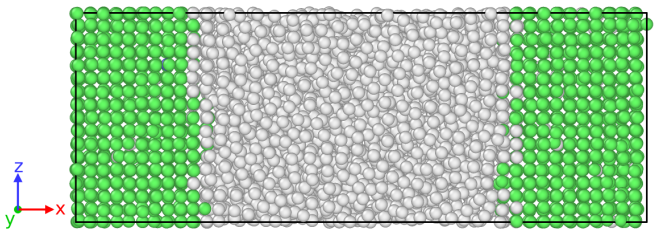


(b) Relaxed simulation box

Figure 2.5.: (a) Initial simulation box of Al with a space in the middle, (b) Relaxed simulation box of Al with liquid and solid phases. (FCC atoms are colored green, liquid and atoms of amorphous solid are colored white.)

After the whole simulation box is relaxed (Fig. 2.5(b)), starts the coexistence period. The system then evolves in an NVE ensemble. In this constant energy ensemble with solid and liquid phases interacting with each other, if the system has a temperature higher than the melting point, then part of the solid phase will melt, convert part of the kinetic energy into potential energy, thus reducing the temperature of the system. Therefore, the system will eventually evolve to a stable solid-liquid coexistence stage. At this time, the system temperature equals the melting temperature. Similarly, if the temperature is lower, part of the liquid phase will solidify to convert its potential energy into kinetic energy. So the system temperature will increase and finally evolve to the melting temperature [71, 73]. Besides common neighbor analysis (CNA) shown in Fig. 2.5, the local order parameter ($Q_6$)[74] is also applied to distinguish between the crystal and liquid phases.

# 3. Results

## 3.1. Force Fields

For AlSi10Mg alloy system, all of the MEAM potentials investigated in this study are listed in Table 3.1, and are marked as P1 to P5 for convenience:

| System | Potential | Abbreviation |
|---|---|---|
| Al | M.I. Pascuet (2015) [75] | P1 |
| | Y.-M. Kim (2009) [76] | P2 |
| | B. Jelinek (2012) [77] | P3 |
| Mg | Y.-M. Kim (2009) (Pure Mg) [76] | P4 |
| | Y.-M. Kim (2009) (Al-Mg system) [76] | P2 |
| | B. Jelinek (2012) [77] | P3 |
| Si | I. Aslam (2019) [78] | P5 |
| | B. Jelinek (2012) [77] | P3 |

Table 3.1.: Potentials used for AlSi10Mg alloy system.

An EAM potential [62] was chosen for the simulation of 304L stainless steel system.

## 3.2. Melting Point

For hysteresis method in this study, cubic simulation boxes containing approximately 4000-5000 atoms are chosen to implement the hysteresis method, which was proved to be large enough to produce reasonable results. Simulation details can be found in Table 3.2. The temperature of the simulation system is controlled by NPT ensemble. Starting from $T_{low}$, the temperature gradually increases to $T_{high}$, then decreases back to $T_{low}$, while the system pressure is kept constant as 1.0 bar. The heating and cooling rate depend on different systems, in order to acquire a complete melting and solidification behavior (low heating and cooling rate) as well as maximum superheating and supercooling (high heating and cooling rate). This range is approximately $0.1 - 5.0 K/ps$ in this study.

| System | Al | Si | Mg | Fe | Cr | Ni | 304L |
|---|---|---|---|---|---|---|---|
| $T_{low}/K$ | 200.0 | 200.0 | 200.0 | 200.0 | 200.0 | 200.0 | 200.0 |
| $T_{high}/K$ | 1400.0 | 2200.0 | 1400.0 | 3200.0 | 2900.0 | 3000.0 | 3200.0 |

Table 3.2.: Simulation setting of hysteresis method.

For coexistence method, simulation boxes containing 5000-10000 atoms were created in this study, which was large enough to produce convincing results [71]. The density ratio and the shifting distance of these systems are in Table 3.3. It should be noted that, for silicon, the density of solid state ($\rho_{273K} = 2.57 g \cdot cm^{-3}$) is larger than liquid state ($\rho_{2000K} = 2.47 g \cdot cm^{-3}$)[79], therefore, no shifting was assigned for silicon system. The

atoms originally in the liquid part were held fixed while the atoms originally in the solid parts were relaxed in the NVT ensemble for 30 ps at $T_{solid}$. After the solid parts were sufficiently relaxed, they were held fixed and an NVT ensemble was applied to the liquid part for 30 ps at $T_{liquid}$. The temperature of the thermostat was not too far from the melting point (about 1.5 times the melting point [71]). Then started the coexistence period for 300 ps in NVE. An ensemble of velocities randomly generated using the Gaussian distribution was applied to all atoms, providing the simulation box with a temperature $T_{equi}$ near the melting point. If appropriate simulation setup was chosen, the system would soon reach a coexistence stage. The temperature of the system at coexistence stage would be the estimated melting point.

| Element | | Al | Mg | Si |
|---|---|---|---|---|
| Density | $\rho_{273K}/g \cdot cm^{-3}$ | 2.70[a] | 1.74[b] | - |
| | $\rho_{1300K}/g \cdot cm^{-3}$ | 2.27[a] | 1.47[b] | - |
| | Density Ratio | 1.19 | 1.18 | - |
| Simulation Box | Original Box Length/Å | 81.0 | 80.0 | 108.6 |
| | Shifting Distance/Å | 7.7 | 7.2 | - |
| Temperature | $T_{solid}$/K | 800.0 | 800.0 | 1500.0 |
| | $T_{liquid}$/K | 1300.0 | 1300.0 | 2200.0 |
| | $T_{equi}$/K | 850.0 | 850.0 | 1600.0 |

[a] Ref.[80]
[b] Ref.[81]

Table 3.3.: Simulation setups of different elements in coexistence method.

### 3.2.1. AlSi10Mg Alloy

For pure Al, Mg, and Si, the melting points calculated using hysteresis method and coexistence method are listed in Table 3.4.

The biases are calculated comparing to the experimental standard melting points of Al, Mg, and Si, respectively, which are $933.47K$ [80], $923K$ [80], and $1687K$ [80]. The bias is defined to be positive if higher than the experimental standard melting point, negative if lower.

The density changes during the heating and cooling process of hysteresis method for pure Al, Mg, and Si systems are shown in Fig. 3.1.

It can be seen from the Fig. 3.1 and the Table 3.4 that the P1, P2, P4, and P5 potentials can give a reliable estimation of the melting point of the corresponding system. But the results of P3 potential were quite away from satisfaction in all systems. What's more, the Al simulated using P3 potential did not solidify under the simulation condition. Many different simulation setups were tested but none of them give a result that solidified. Therefore, no result is reported for the P3 using hysteresis method. Moreover, the P3 potential was very unstable at high temperature compared to other potentials, which means a shorter simulation timestep must be used (0.2 fs the longest) to avoid blow up of simulation box. These results show that the P3 potential is not suitable for later directional solidification study.

In summary, the only potential (P3) containing Al, Si, and Mg failed to predict the behavior of the simulation system during the melting and solidification process. Therefore,

| System | Potential | Method | Result/K | Bias |
|---|---|---|---|---|
| Al | P1 | Hysteresis | 892.50 | -4.39% |
| | | Coexistence | 982.11 | +5.21% |
| | P2 | Hysteresis | 888.17 | -4.85% |
| | | Coexistence | 921.69 | -1.26% |
| | P3 | Hysteresis | - | - |
| | | Coexistence | 1299.33 | +39.19% |
| Mg | P4 | Hysteresis | 898.42 | -2.66% |
| | | Coexistence | 954.87 | +3.45% |
| | P2 | Hysteresis | 882.60 | -4.38% |
| | | Coexistence | 946.77 | +2.58% |
| | P3 | Hysteresis | 748.09 | -18.95% |
| | | Coexistence | 1150.61 | +24.66% |
| Si | P5 | Hysteresis | 1185.12 | -29.75% |
| | | Coexistence | 1687.4 | +0.02% |
| | P3 | Hysteresis | 1590.03 | -5.75% |
| | | Coexistence | 1376.35 | -18.41% |

Table 3.4.: The melting points of Al, Mg, and Si systems estimated using hysteresis method and coexistence method.

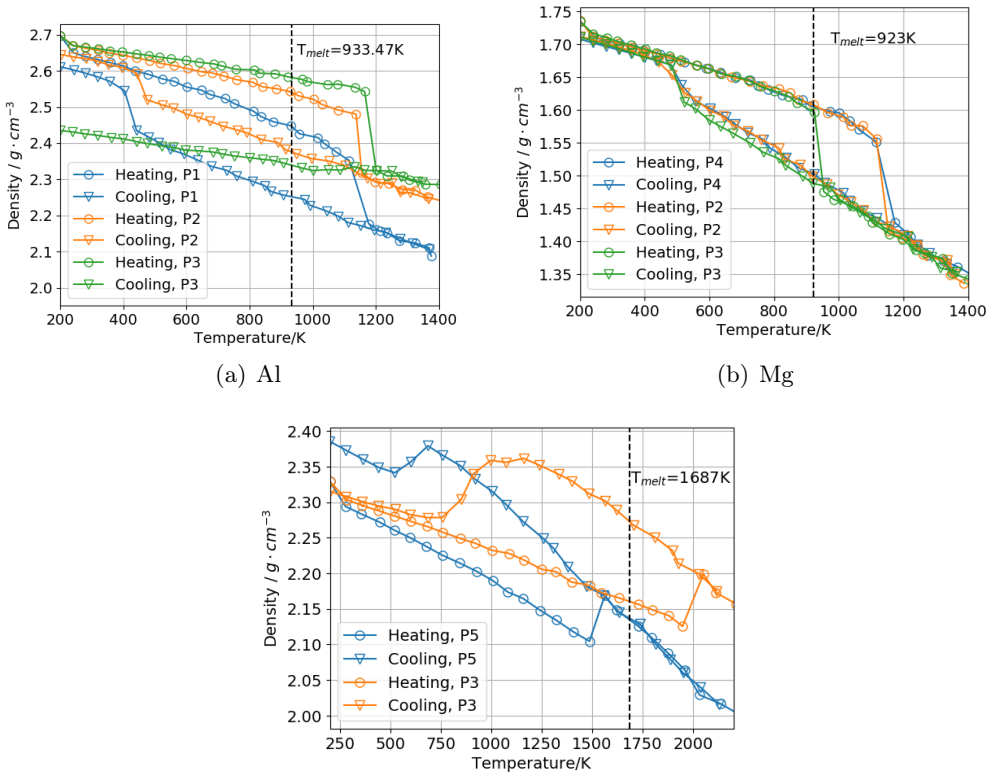


(a) Al

(b) Mg

(c) Si

Figure 3.1.: Density changes of Al, Mg, and Si systems using different potentials.

till now there exists no single MEAM potential that can perform the simulation of AlSi10Mg alloy during the melting and directional solidification processes.

### 3.2.2. 304L Stainless Steel

The density change of Al, Cr, and Ni during heating and cooling process of hysteresis method are shown in Fig. 3.2.

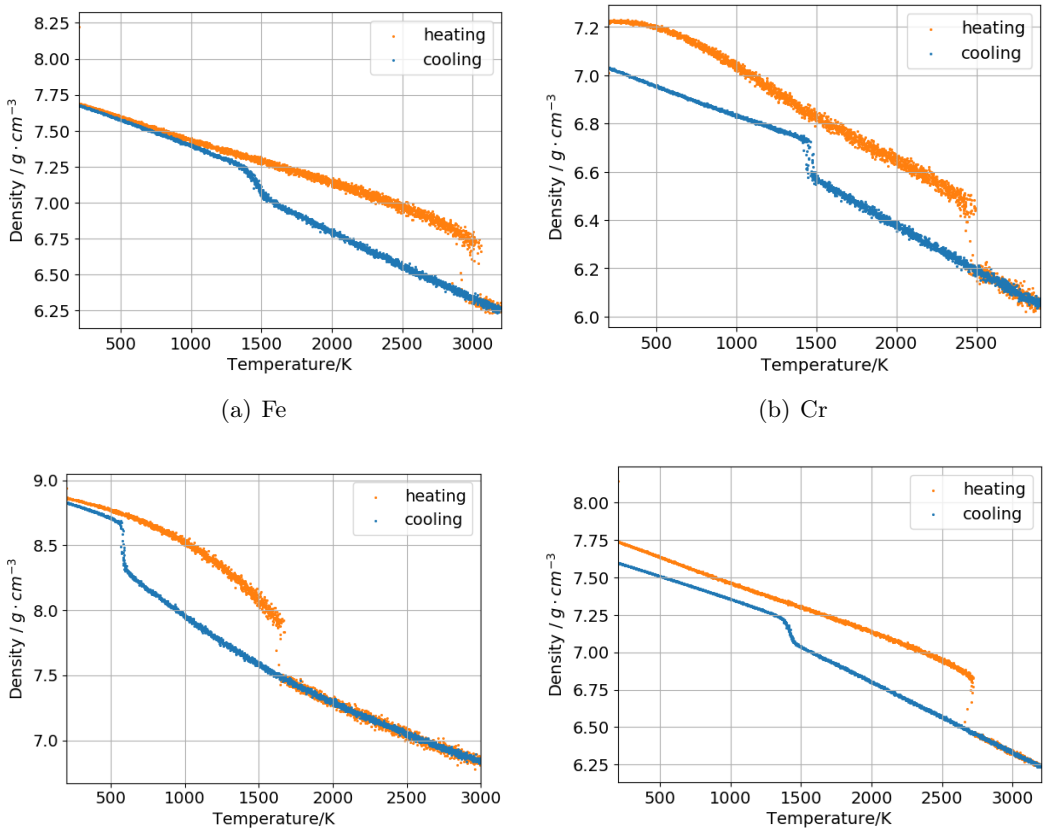


(a) Fe (b) Cr

(c) Ni (d) 304L

Figure 3.2.: Density change of main elements in 304L stainless steel.

In Fig. 3.2(b) and Fig. 3.2(d), the difference of density before melting and after solidification is because of the change of crystal structure. For Cr, the initial BCC structure turned into an FCC structure with grain boundaries and twin boundaries. For 304L, the final product after solidification has multiple phases (FCC, BCC, and HCP) and plenty of grain boundaries.

The estimation of melting point of Fe, Cr, and Ni using coexistence method has already been done by the author of the potential [62]. So only the estimation of melting point of 304L was performed using coexistence method in this study. The results in Table 3.5 indicate that the prediction of the melting point of Cr matches the experimental value very well. On the contrary, the prediction of the melting points of Fe, Cr, and Ni are away from the experimental data. The biases can be up to approximately 30%. However, all of these results show good stability throughout the whole melting and solidification process, which

means this potential is acceptable for melting and solidification simulation.

| System | Method | Result/K | Bias |
|---|---|---|---|
| Fe | Hysteresis | 2379 | +31.36% |
| | Coexistence | 2399[a] | +32.47% |
| Cr | Hysteresis | 2022 | -5.34% |
| | Coexistence | 2133[a] | +0.14% |
| Ni | Hysteresis | 1255 | -27.37% |
| | Coexistence | 1346[a] | -22.11% |
| 304L | Hysteresis | 2171 | +(26.00-29.77)% |
| | Coexistence | 2150 | +(24.78-28.51)% |

[a] Ref.[62]

Table 3.5.: The melting points of Fe, Cr, Ni, and 304L estimated using the MD simulation method.

For the comparison of these two methods estimating melting point in MD, the hysteresis method has lower accuracy than the coexistence method. Because it needs an estimation of both degree of superheating and degree of supercooling, which may introduce error by manually choosing temperature turning point. Moreover, there is no guarantee that a "maximum superheating/supercooling" is reached. The coexistence method is more accurate but harder to perform, as the expansion or shrinkage of the simulation box caused by density change during the melting needs to be considered. Improper handling of this expansion might cause error or failure.

## 3.3. Directional Solidification

To the best of our knowledge, currently, there is no EAM or MEAM potential that can reliably describe the behavior of the Al-Si-Mg system during solidification. Jelinek's MEAM potential [77] failed to reproduce the behavior of this system at high temperature. So in this study, only an Al-Mg system was studied to reveal partial properties of AlSi10Mg alloy, as well as the temperature dependence of the directional solidification behavior. The chemical compositions of this Al-Mg system are listed in Table 3.6. Based on the standard [82], the chemical compositions of 304L stainless steel in this study are prescribed as Table 3.6.

| System | Al-Mg | | 304L | | |
|---|---|---|---|---|---|
| Element | Al | Mg | Fe | Cr | Ni |
| at % | 90.0 | 10.0 | 70.0 | 21.0 | 9.0 |

Table 3.6.: Chemical compositions of 304L in atomic percent.

Directional solidification in AM process in the real world is complicated because of the complex thermal evolution of the system. So in this study, only a simple directional solidification caused by one-dimensional temperature gradient was considered due to the limitation of the MD simulations.

To study the rapid directional solidification process at the atomic scale in the transition area, a simulation box with the size of about $30 \times 30 \times 30(nm^3)$ containing about 2.4M atoms was created, in which 21.0% of Cr and 9.0% of Ni randomly distributed in FCC structure Fe (Fig. 3.3(a)). For the Al-Mg system, a smaller simulation box with the size

of $10 \times 10 \times 10(nm^3)$ was chosen, which contains about 62500 atoms with 10.0% of Mg randomly distributed.

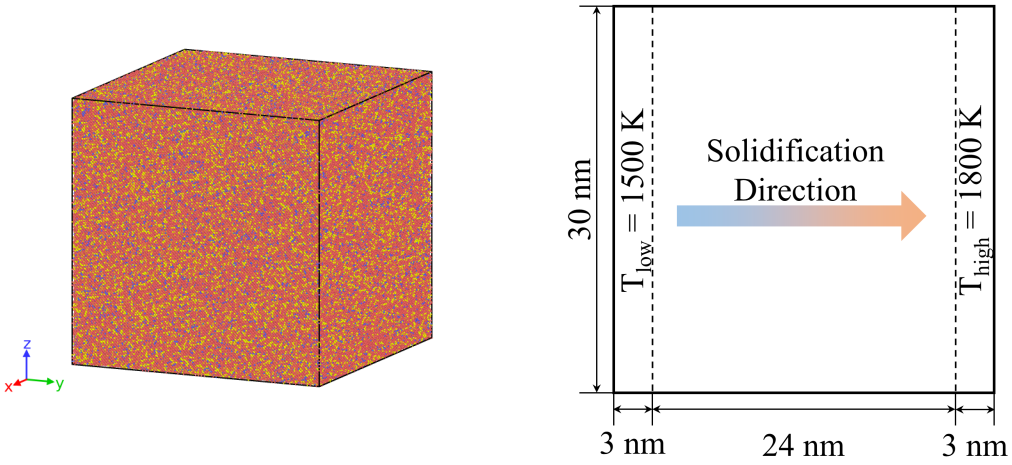


(a) (b)

Figure 3.3.: (a) Initial simulation box with FCC structure, in which red atoms are Fe, yellow atoms are Cr, and blue are Ni. (b) Simulation setup for the directional solidification.

The simulation of directional solidification mainly consists of two steps:

1. Melting. The simulation box was heated above the melting point to prepare a homogeneous molten phase. The whole simulation box was kept at 2700K (1400K for Al-Mg system) using NPT ensemble for 150 ps with a timestep of 3 fs. Temperature and pressure were controlled by Nose-Hoover thermostat and Parrinello-Rahman barostat respectively. Periodic boundary conditions were applied to all three directions.

2. Directional solidification. The simulation box was divided into three regions (as shown in Fig. 3.3(b)) after melting. The left region with a thickness of 3 nm was assigned as low temperature region and kept at a constant temperature of $T_{low} = 1500K$, while the region on the right with a thickness of 3 nm as high temperature region kept at constant $T_{high} = 1800K$. The choice of the temperature will be discussed in Section 3.3.2. They were kept at a constant temperature using Langevin thermostat, while the middle region was not controlled by any thermostat to create a temperature gradient. An NVE ensemble was applied to the whole simulation box. The boundary along the solidification direction was changed to non-periodic before the directional solidification stage.

### 3.3.1. Al-10 at % Mg

As discussed in section 3.2.1, there is no single MEAM potential that can simulate the melting and solidification process of AlSi10Mg alloy. So P2 potential for the Al-Mg system was chosen to study partial properties of the alloy.

Simulation setups with several different $T_{low}$ and $T_{high}$ were chosen, in order to find out an optimal setup for directional solidification. The simulation time is 1 ns. Most of the simulations reached a stable state within simulation time 1 ns where no obvious fluctuation in the structure and physical properties can be observed. Solid with amorphous structure like grain boundaries takes up only a limited percentage in the final product, so the percentage of the crystal structure can indicate the solid ratio in the final product. Considering only the percentage of the crystal structure (FCC+HCP) of the final configurations, the results of different simulation setups are listed in Fig. 3.4.

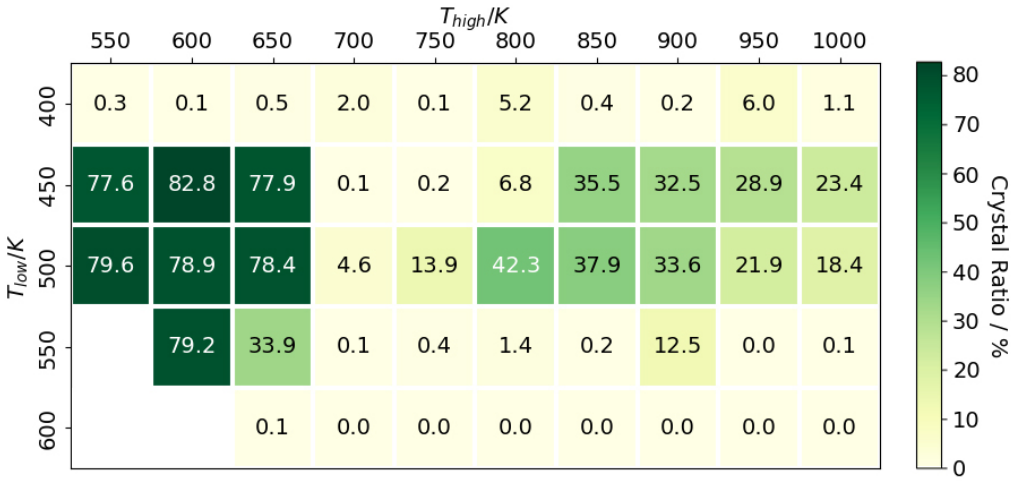


Figure 3.4.: Results of directional solidification of Al-10 at % Mg system.

It can be seen from the results that only the simulations with temperature setup in a limited range (approximately 450-500 K) can experience solidification within 1 ns. There are two possibilities that no solidification occurred during the simulation within 1 ns. One reason is that the temperature setup is too high for solidification, i.e. the critical radius for embryos growing into nucleus is too large, for example when $T_{low} = 600K$. Another reason is that the low temperature limited the diffusion of atoms, so the process of nucleation and growth was very slow, for example when $T_{low} = 400K$. It is possible that the crystal ratio would continue to grow after 1 ns, but this is not efficient and will cost unnecessary computational power. This phenomenon is in agreement with the fact discussed in 2.2.1 that there exists a critical degree of supercooling for the highest nucleation rate. When $T_{low} = 450 - 500K$ and $T_{high} = 800 - 1000K$, the solidification can occur and reach a stable state within 1 ns. But in these simulations, the solidification front only traveled to the middle of the simulation box and stopped there, which is because the temperature near the high temperature was too high for solidification.

It should be noted that when $T_{low} = 450 - 550K$ and $T_{high} = 550 - 650K$, the crystal percentages for these simulations are very high and the solidification happened in the whole simulation box. But the temperature difference between $T_{low}$ and $T_{high}$ in these simulations are not high enough, which makes it almost impossible to tell the difference between homogeneous solidification and directional solidification. For instance, when $T_{low} = 500K$ and $T_{high} = 550K$, the nucleation occurred in high temperature region first, then propagated towards low temperature region, which did not go as planned.

As Al-10 at % Mg alloy is not commonly used in AM, no further study of this system was carried out.

### 3.3.2. 304L Stainless Steel

The choice of simulation temperature was inspired by Bahramyan et al. [30], in their paper they chose 1550-1850 K "based on the phase diagram melting temperature range for SS 316 L of 1663 K–1713 K". However, according to the relationship of simulation temperature and crystal ratio discussed above in 3.3.1, this temperature range, which is approximately $0.15 - 0.30\ T_m$ lower than $T_m$ ($T_m \approx 2180K$ [62]), is actually the temperature around the critical degree of supercooling for highest nucleation rate. Thus temperature range of 1500-1800 K was chosen in this study, which was later proved to be an appropriate choice.

The density change during the whole simulation process is shown in Fig. 3.5. The system was totally melted after about 50 ps in the melting stage, then stayed in equilibrium till the next stage. The density increased during the directional solidification stage, which suggests a phase change from liquid to solid. After approximately 750 ps in the directional solidification stage, the density was stable around 6.95 $g/cm^{-3}$.

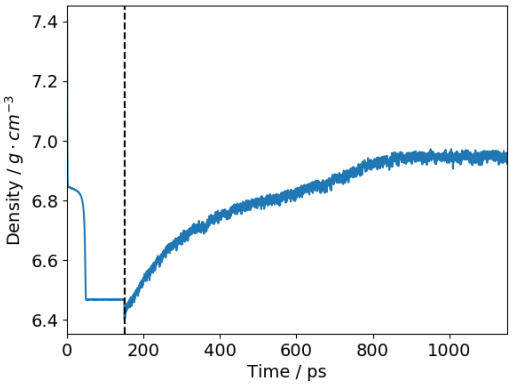


Figure 3.5.: Density change of 304L simulation system during the whole simulation process. The dashed line indicates the change from the melting stage to the directional solidification stage.

The temperature change during the directional solidification process is plotted in Fig. 3.6(a). The temperature of every region reached a stable stage after about 800 ps. For region 12-18 nm and region 18-27 nm, there existed a slight temperature increase at approximately 400-600 ps. This might be caused by the exotherm of solidification. As shown in Fig. 3.6(b), the simulation box reached the designated temperature gradient of 10 $K/nm$, the temperature gradient in the middle region was approximately 15 $K/nm$, which indicates a reasonable temperature environment for directional solidification.

The process of crystal growth during the directional solidification of the 304L system is demonstrated in Fig. 3.7 using various methods. Atoms in different phases are colored using common neighbor analysis (CNA), where FCC atoms are green, HCP atoms are red, BCC atoms are blue, and atoms in liquid and amorphous solid are white.

Nuclei in low temperature region can be observed at 250 ps, indicating a heterogeneous solidification. These nuclei continued to grow and form small grains, then new nuclei formed on the surface of these grains and grew. The solidification front traveled from low

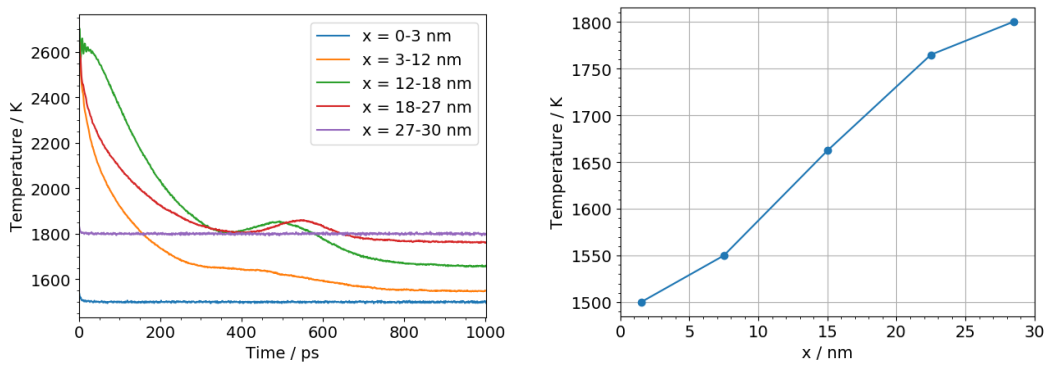


(a) Temperature changes with time in every region during the directional solidification stage.

(b) Temperature of every region at 1 ns of the directional solidification stage.

Figure 3.6.: The temperature change of simulation system.

temperature region on the left towards high temperature region on the right. The solid has mainly FCC structure which indicates the formation of an austenitic steel.

The ratio of every structure changing with time is shown in Fig. 3.8(a). The ratio of FCC and HCP structure began to increase at about 200 ps and reached stable at about 750 ps, while the increasing period for BCC structure is about 200-450 ps. At 1 ns, the ratio of FCC, HCP, and BCC structure are 36.7%, 11.1%, and 2.4% respectively.

Ratios of elements in different crystal structures are also plotted in Fig. 3.8(b-d). These ratios went stable at the beginning of grain growth. The dashed orange line in the figures indicates the average percentage of this element in the whole simulation box. It can be seen from these figures that the Fe atoms tended to concentrate in FCC and HCP structures, while Cr atoms in BCC. Ni atoms tended to be enriched in the amorphous structure, namely segregation in grain boundaries. This concentration of elements cannot be easily observed in simulation, since these percentage differences are only 1-2%.

It can be observed in Fig. 3.7 that the grains grown in the first place in the low-temperature region are finer than those grew later in other regions. Here choose the number of atoms in every grain as grain size, then take the logarithm of the number of atoms for ease of demonstration. The results are illustrated in Fig. 3.9. As can be seen that the grains that emerged later are bigger in size and fewer in number.

## 3.4. Uniaxial Tensile Test

To study the deformation mechanics and the mechanical properties of the solidified structure, uniaxial tensile tests were performed on the final configuration of the directional solidification product. The final configuration was taken from the directional solidification product when the solidification process reaches a stable stage. The temperature for uniaxial tensile tests is chosen as 300 K, so this final configuration was equilibrated under 300 K for 100 ps using NPT ensemble to stabilize the atoms from the high temperature of the directional solidification. A strain rate of $10^{10}(s^{-1})$ was applied to directions parallel to and perpendicular to the solidification direction respectively.

After being kept under 300 K for 100 ps, the simulation box experienced further solidification and had more distinct phases. The ratio of FCC, HCP, and BCC structure increased

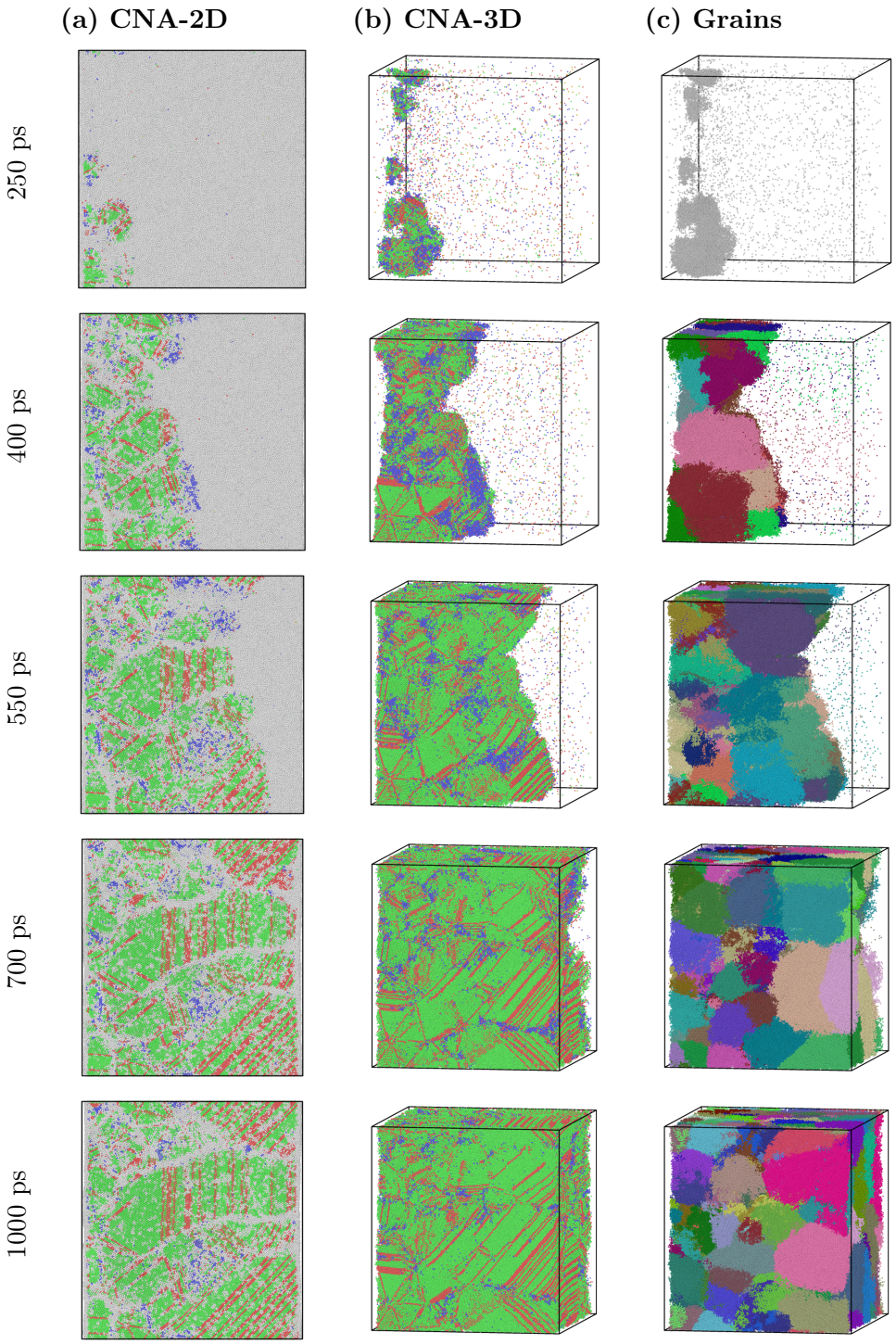


Figure 3.7.: Crystal growing process during directional solidification. (a) CNA-2D are the front views of the simulation box with atoms colored by OVITO CNA. (b) CNA-3D are the perspective views of the simulation box with all liquid and non-crystal atoms removed. (c) In "Grains" atoms are colored with respect to different grains.

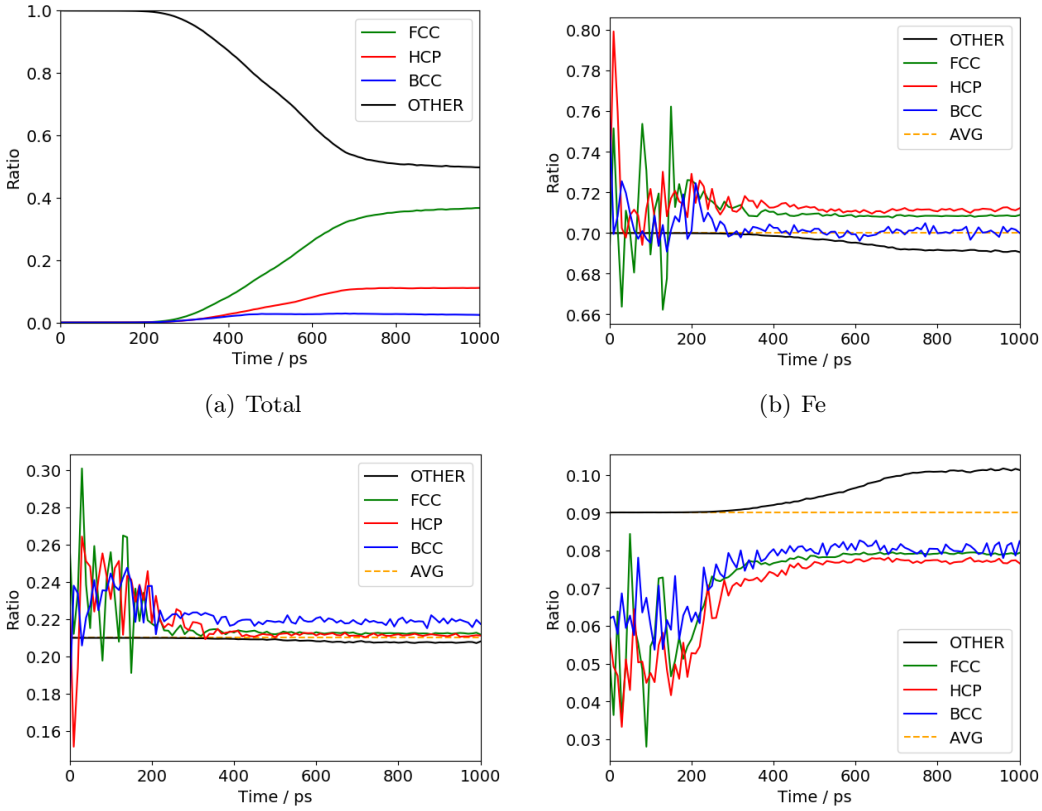


(a) Total (b) Fe

(c) Cr (d) Ni

Figure 3.8.: Element percentage in different structures during the directional solidification stage.

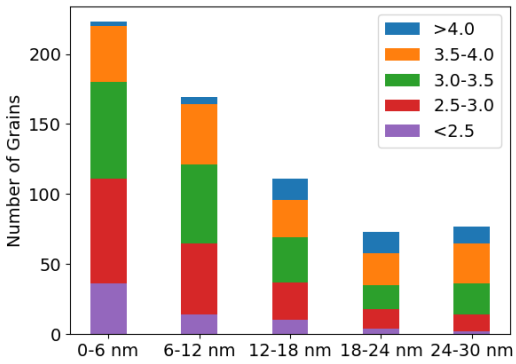


Figure 3.9.: The number of grains of different sizes in every region. Grain size is represented by the logarithm of the number of atoms in the grain.

to 58.5 %, 19.7 %, and 3.9 %, respectively.

The stress-strain relationship of two loading directions during the uniaxial tensile test are shown in Fig. 3.10.

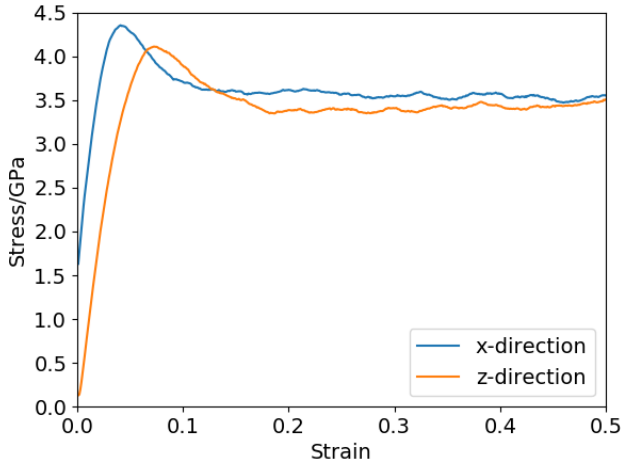


Figure 3.10.: The deformation of simulation box under uniaxial tensile.

As shown in the figure, the ultimate tensile strength in x-direction was slightly larger than in z-direction, while their evolutions were generally the same. Note that there was a residual stress of about 1.6 $GPa$ in the x-direction. Studies show that the residual stress in certain parts of the sample made by SLM can be comparable to the yield strength [31, 83]. In this simulation, the possible cause for this residual stress in x-direction could be the stress accumulated during directional solidification.

The ratio changes of every structure during deformation are shown in Fig. 3.11. The figures are zoomed in for better details. The trends of the ratio changing with strain in these two directions are roughly the same. The increase of amorphous structure percentage indicates the destruction of previous crystal structures. The ratio of FCC structure experienced a monotonically decreasing, which means the FCC structure transformed into another structure. The decrease of HCP ratio and the increase of BCC ratio can be explained as the martensitic transformation in TRIP steel, which is $\gamma(FCC) \rightarrow \varepsilon(HCP) \rightarrow \alpha'(BCC)$.

A closer look into the crystal structure is needed to study this martensitic transformation in TRIP steel. Fig. 3.12 and Fig. 3.13 show the zoomed-in views of the snapshots during the tensile test.

Between Fig. 3.12(a) and Fig. 3.12(b), a large bunch of stacking faults and twin boundaries were formed as HCP structures in the original FCC structure. Later part of these faults with HCP structure transformed into BCC structure under tensile load, which is the BCC structure with irregular shape in the middle of stacking fault and grain boundaries shown in Fig. 3.12(d). This FCC-HCP-BCC transformation is in agreement with the martensitic transformation in TRIP steels [36, 37, 38].

A larger area of martensitic transformation under tensile load in z-direction is shown in Fig. 3.13. On the top there was a small area of atoms that went through the whole FCC-HCP-BCC process: HCP formed from FCC (Fig. 3.13(b)), then turned into BCC (Fig. 3.13(c)). But the large area of BCC structure on the bottom was transformed directly from HCP. It can be seen in Fig. 3.13(b) that the one layer of FCC atoms that were in the

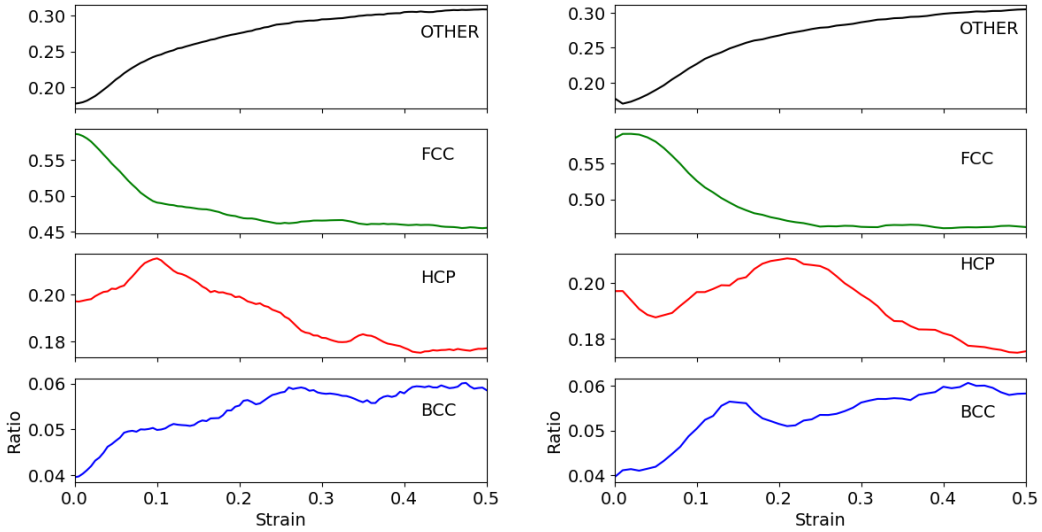


(a) Loading on x-direction (b) Loading on z-direction

Figure 3.11.: Structure change during the tensile test.

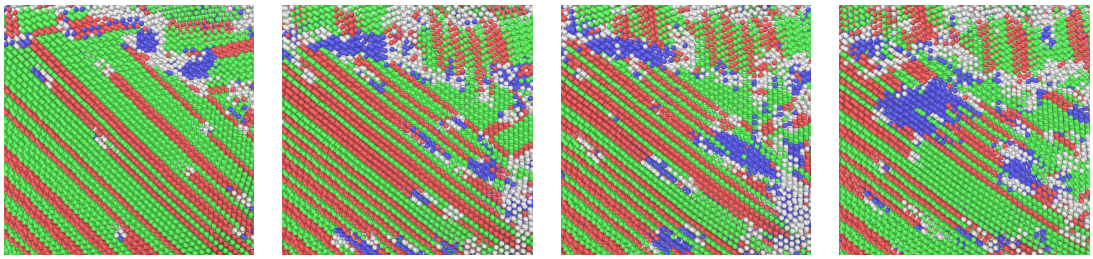

(a) 5.0% (b) 16.0% (c) 18.0% (d) 21.0%

Figure 3.12.: CNA when the tensile load is applied on x-direction.

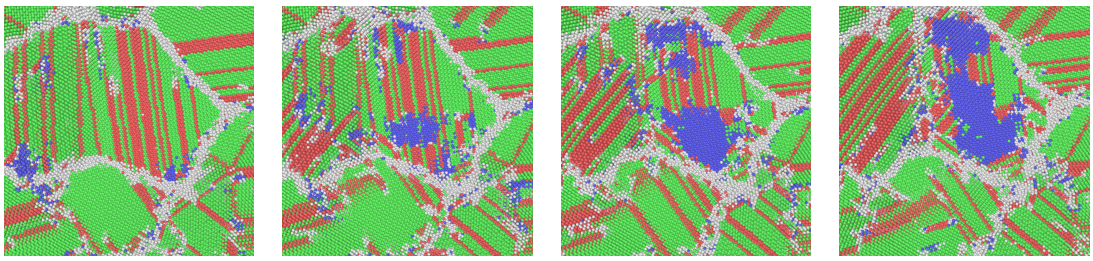

(a) 10.0% (b) 13.0% (c) 15.0% (d) 18.0%

Figure 3.13.: CNA when the tensile load is applied on z-direction.

middle of HCP before still remained unchanged. After further deformation, this layer of FCC atoms accompanying other FCC atoms in the neighborhood transformed into BCC structure (Fig. 3.13(c)). Fig. 3.13(d) shows that the BCC structure formed through two different mechanisms joined together along with the HCP structure.

## 3.5. Thermal Shock

A thermal shock study was performed on the final configuration of the directional solidification product. The thermal shock loading caused by heat or electrons was simplified into such a process that a thin layer of the final product was heated (thermal shocked region) while the rest of the simulation box remained unheated.

To achieve this, in the 304L system, the simulation box was firstly evenly divided into 100 thin layers in order to monitor temperature and normal stress along the x-direction. At one end, 10 layers of atoms were chosen as thermal shock region, while at the other end 5 layers were kept fixed at their original position throughout the simulation. Then the whole system was equilibrated at 1 K for 100 ps using NPT ensemble and periodic boundary conditions at all directions. This is for the simplification of discussion and convenience of simulation. After equilibrium, the initial temperature (1500 K) of thermal shock was applied to the thermal shock region by velocity rescaling. The whole system was then allowed to evolve freely in an NVE ensemble. Periodic boundary conditions were only applied to directions parallel to the thermal shock direction to get rid of boundary effects.

Stress wave induced by thermal shock is a common phenomenon. The sudden expansion of the thermal shock region caused the first main normal stress peak at the beginning of the simulation. Fig. 3.14 shows the propagation of normal stress ($\sigma_x$) along the thermal shock direction. After this stress wave, the stress value returned to a small fluctuation around 0. It can be inferred from the figure that the speed of the stress wave propagation is about 6150 m/s, which is in good agreement with the speed of sound in steel (6000 m/s) [84].

After the stress wave peak hit the fixed region at about 4.0-4.5 ps, it was reflected back to the simulation box by the fixed region. This phenomenon is not discussed in this study.

The heat propagation after thermal shock can be seen in Fig. 3.15. There is no significant difference between these two results where thermal shock happened in different directions. The temperature in the thermal shock region dropped gradually, and the heat diffused towards the other end of the simulation box.

According to observation and CNA, no obvious change in nano-structure can be found after thermal shock. This indicates that the abrupt reheating in the neighboring regions during SLM simulated by thermal shock in this study does not affect the structure and properties of the solidified region. This is contrary to the results of the study of Yang et al. [7] that reheating caused by laser scanning in the neighborhood can result in multiple types of martensite, which could indicate that the idea of simulating this reheating process by thermal shock in this study is inappropriate.

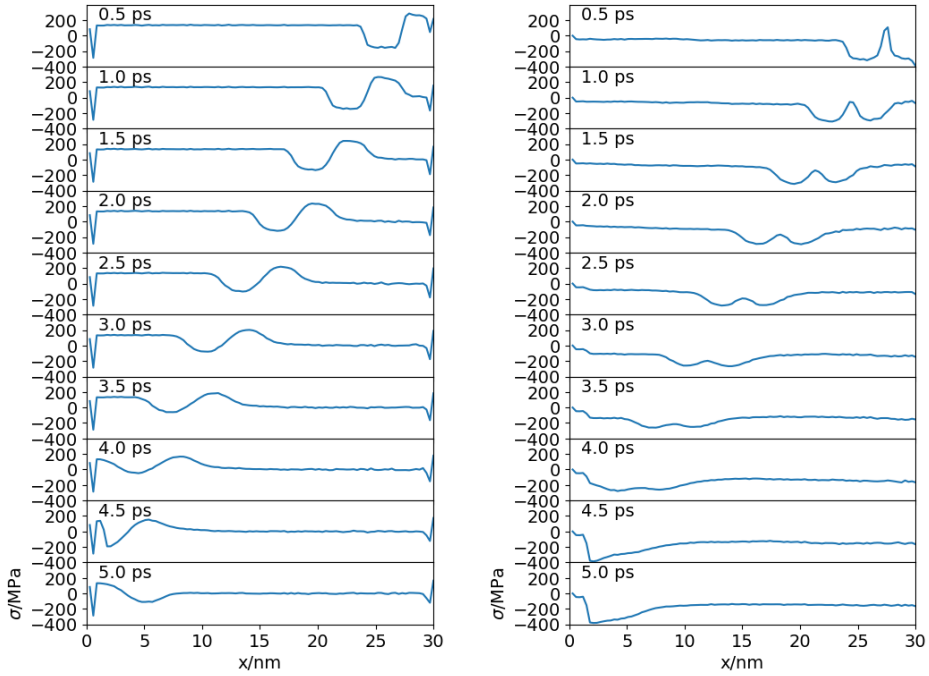


(a) x-direction (b) z-direction

Figure 3.14.: Evolution of the normal stress $\sigma_x$ distributions along thermal shock direction.

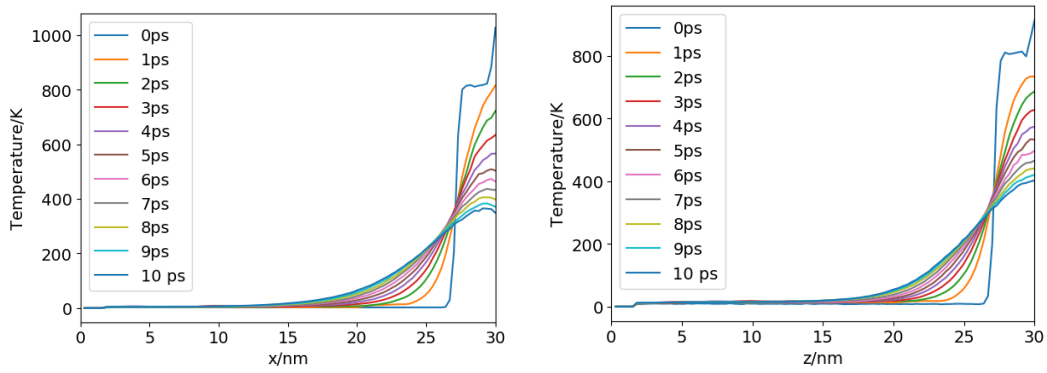


(a) x-direction (b) z-direction

Figure 3.15.: Temperature change along thermal shock direction.

# 4. Conclusions and Outlook

In this study, a serial of MD simulations was performed to investigate the directional solidification of alloys for additive manufacturing. The melting point of each element in alloy systems simulated using different potentials was estimated using hysteresis and coexistence methods. The feasibility of simulating the AlSi10Mg alloy using existing MEAM potential was discussed, which is denied because of biases in melting temperature, instability at high temperature, and the inability of solidification of Al element. Simulations of directional solidification of Al-10 at % Mg system under different temperature setups were conducted, the results of which were analysed by the CNA. A successful directional solidification of the 304L stainless steel system was performed, followed by an observation of the nanostructure of the final configuration. Uniaxial tensile tests and thermal shock tests were also performed on this final configuration. The following conclusions can be drawn from the previous discussions:

1. There exists an optimal temperature range for highest nucleation rate.
2. Directional solidification caused heterogeneity in nanostructure.
3. The ultimate tensile strength was higher in x-direction than in z-direction. A residual stress can be observed in x-direction.
4. TRIP effect and martensitic transformation was observed during the uniaxial tensile test.
5. Thermal shock simulated in this study did not affect the structure and properties of directional solidified 304L stainless steel.

This paper can be considered as a preliminary delving for future study on directional solidification of other alloys. Further improvement can be made in the following ways.

Firstly, the directional solidification study discussed in this paper can be extended to other alloy systems if potential that can mimic the system's behavior around the melting point is available. There are many other alloys popular for AM, such as AlSi10Mg, Ti6Al4V, stainless steel 316L, etc. However, to the best of the author's knowledge, currently, there's no reliable MEAM potential that can reproduce the nucleation and solidification process of AlSi10Mg alloy near the melting point. This perhaps is because of the precipitates during the solidification like $\beta'$ phase and $\beta''$ phase have complex nano-structure [85, 86], which makes the description of precipitation using traditional MEAM potential difficult. Recently, Kobayashi et al. [87] developed a neural network potential for the ternary Al-Mg-Si system. The precipitate energy results calculated using this potential are in good agreement with DFT results. This could be a solution for describing the directional solidification behavior of the Al-Mg-Si system. For Ti6Al4V, EAM potential for this ternary system is also unavailable. Potentials for Ti-Al [88], Ti-V [89], Al-V [53] binary systems are available, though. If enough *ab initio* data are available, there is the possibility that the MEAM potentials s for the Ti-Al-V system can be interpolated using these binary potentials [90, 91].

But this is beyond the scope of this study. The main components of 316L stainless steel are Fe, Cr, Ni, and Mo. Same as Ti6Al4V discussed above, EAM potential describes the Fe-Cr-Ni system [62] is available but not available for Fe-Cr-Ni-Mo system. Although Mo in 316L is only 2-3% weight percent, lack of Mo can lead to no cellular structure after directional solidification [30].

Secondly, better computational performance means that a larger simulation box containing more atoms can be simulated in the same time period, which suggests more information can be obtained from the simulation. Some precipitation can be with the size of tens of nanometers or larger, an even larger simulation box is needed to study the formation of them. One important way of accelerating the large-scale MD simulations is using GPU acceleration. Shibuta et al. [92] developed a parallel GPU code for MD and studied the heterogeneity in homogeneous nucleation of a cubic simulation box with an edge length of $0.24\mu m$ containing one billion atoms.

Thirdly, multiscale modeling and combination of other methods can also be a way of improvement. The phase-field method is limited by its inability to reproduce nucleation behavior, whereas the MD method is limited by its expensive computational cost in a large simulation box. With the help of the multiscale modeling method, it is possible that simulation of nucleation process using MD combines with the simulation of dendritic structure growth on large scale using phase field. Fu et al. [93] demonstrated the feasibility of bridging the multi-phase field model with MD, which enabled better predictions of melting, solidification, and phase transition process. Moreover, if the MD simulation is connected to FEM and CFD simulation on a macroscale [12], the simulation will be one more step closer to the real world by introducing a multi-dimension temperature gradient. Ninpetch et al. [10] conducted a CFD simulation of temperature behavior during the SLM process, including complex temperature gradient around the melt pool.

# A. Acronyms and Abbreviations

| | |
|---|---|
| AM | additive manufacturing |
| BCC | body-centered cubic |
| CNA | common neighbor analysis |
| EAM | embedded-atom method |
| FCC | face-centered cubic |
| HCP | hexagonal close-packed |
| MD | molecular dynamics |
| MEAM | modified embedded-atom method |
| SLM | selective laser melting |
| TRIP | transformation induced plasticity |
| UTS | uniaxial tensile strength |

# Bibliography


[1] R. E. Reed-Hill, R. Abbaschian, and R. Abbaschian, *Physical metallurgy principles*, vol. 17. Van Nostrand New York, 1973.

[2] I. Gibson, D. W. Rosen, B. Stucker, and M. Khorasani, *Additive manufacturing technologies*, vol. 17. Springer, 2021.

[3] W. E. Frazier, "Metal additive manufacturing: a review," *Journal of Materials Engineering and performance*, vol. 23, no. 6, pp. 1917–1928, 2014.

[4] M. Islam, T. Purtonen, H. Piili, A. Salminen, and O. Nyrhilä, "Temperature profile and imaging analysis of laser additive manufacturing of stainless steel," *Physics Procedia*, vol. 41, pp. 835–842, 2013.

[5] N. T. Aboulkhair, M. Simonelli, L. Parry, I. Ashcroft, C. Tuck, and R. Hague, "3d printing of aluminium alloys: Additive manufacturing of aluminium alloys using selective laser melting," *Progress in materials science*, vol. 106, p. 100578, 2019.

[6] P. Kobryn and S. L. Semiatin, "The laser additive manufacture of ti-6al-4v," *Jom*, vol. 53, no. 9, pp. 40–42, 2001.

[7] J. Yang, H. Yu, J. Yin, M. Gao, Z. Wang, and X. Zeng, "Formation and control of martensite in ti-6al-4v alloy produced by selective laser melting," *Materials & Design*, vol. 108, pp. 308–318, 2016.

[8] D. Gu, *Laser additive manufacturing of high-performance materials*. Springer, 2015.

[9] S. Liu and Y. C. Shin, "Additive manufacturing of ti6al4v alloy: A review," *Materials & Design*, vol. 164, p. 107552, 2019.

[10] P. Ninpetch, P. Kowitwarangkul, S. Mahathanabodee, P. Chalermkarnnon, and P. Rattanadecho, "Computational investigation of thermal behavior and molten metal flow with moving laser heat source for selective laser melting process," *Case Studies in Thermal Engineering*, vol. 24, p. 100860, 2021.

[11] C. Panwisawas, Y. T. Tang, and R. C. Reed, "Metal 3d printing as a disruptive technology for superalloys," *Nature communications*, vol. 11, no. 1, pp. 1–4, 2020.

[12] W. E. King, A. T. Anderson, R. M. Ferencz, N. E. Hodge, C. Kamath, S. A. Khairallah, and A. M. Rubenchik, "Laser powder bed fusion additive manufacturing of metals; physics, computational, and materials challenges," *Applied Physics Reviews*, vol. 2, no. 4, p. 041304, 2015.

[13] Y. Lee and W. Zhang, "Mesoscopic simulation of heat transfer and fluid flow in laser powder bed additive manufacturing," in *International solid free form fabrication symposium, Austin*, pp. 1154–1165, 2015.

[14] J. H. K. Tan, S. L. Sing, and W. Y. Yeong, "Microstructure modelling for metallic additive manufacturing: A review," *Virtual and Physical Prototyping*, vol. 15, no. 1, pp. 87–105, 2020.

[15] A. F. Voter, "Introduction to the kinetic monte carlo method," in *Radiation effects in solids*, pp. 1–23, Springer, 2007.

[16] B. Chopard and M. Droz, *Cellular automata*, vol. 1. Springer, 1998.

[17] D. M. Stefanescu, *Science and engineering of casting solidification*. Springer, 2015.

[18] T. M. Rodgers, J. D. Madison, and V. Tikare, "Simulation of metal additive manufacturing microstructures using kinetic monte carlo," *Computational Materials Science*, vol. 135, pp. 78–89, 2017.

[19] R. Wang, Y. Liu, and D. Q. Wei, "Microstructures in solidification simulation of electron beam scanning with mc in molten pool," in *Advanced Materials Research*, vol. 898, pp. 168–172, Trans Tech Publ, 2014.

[20] W. J. Boettinger, J. A. Warren, C. Beckermann, and A. Karma, "Phase-field simulation of solidification," *Annual review of materials research*, vol. 32, no. 1, pp. 163–194, 2002.

[21] S. Sahoo and K. Chou, "Phase-field simulation of microstructure evolution of ti–6al–4v in electron beam additive manufacturing process," *Additive manufacturing*, vol. 9, pp. 14–24, 2016.

[22] X. Gong and K. Chou, "Phase-field modeling of microstructure evolution in electron beam additive manufacturing," *Jom*, vol. 67, no. 5, pp. 1176–1182, 2015.

[23] D. C. Rapaport, *The art of molecular dynamics simulation*. Cambridge university press, 2004.

[24] B. S. Daan Frenkel, *Understanding Molecular Simulation: From Algorithms to Applications (2nd Edition)*. London: Academic Press, 2001.

[25] B. Wenger, P. K. Nayak, X. Wen, S. V. Kesava, N. K. Noel, and H. J. Snaith, "Consolidation of the optoelectronic properties of ch 3 nh 3 pbbr 3 perovskite single crystals," *Nature communications*, vol. 8, no. 1, pp. 1–10, 2017.

[26] J. Parajuli, "Metal segregation during the solidification of titanium-aluminum alloys for 3d printing applications," Master's thesis, Louisiana Tech University, 2018.

[27] S. Kurian and R. Mirzaeifar, "Selective laser melting of aluminum nano-powder particles, a molecular dynamics study," *Additive Manufacturing*, vol. 35, p. 101272, 2020.

[28] J. Nandy, N. Yedla, P. Gupta, H. Sarangi, and S. Sahoo, "Sintering of alsi10mg particles in direct metal laser sintering process: a molecular dynamics simulation study," *Materials Chemistry and Physics*, vol. 236, p. 121803, 2019.

[29] A. Mahata and M. A. Zaeem, "Effects of solidification defects on nanoscale mechanical properties of rapid directionally solidified al-cu alloy: A large scale molecular dynamics study," *Journal of Crystal Growth*, vol. 527, p. 125255, 2019.

[30] M. Bahramyan, R. T. Mousavian, J. G. Carton, and D. Brabazon, "Nano-scale simulation of directional solidification in twip stainless steels: A focus on plastic deformation mechanisms," *Materials Science and Engineering: A*, vol. 812, p. 140999, 2021.

[31] L. Liu, Q. Ding, Y. Zhong, J. Zou, J. Wu, Y.-L. Chiu, J. Li, Z. Zhang, Q. Yu, and Z. Shen, "Dislocation network in additive manufactured steel breaks strength–ductility trade-off," *Materials Today*, vol. 21, no. 4, pp. 354–361, 2018.

[32] F. Wang, S. Williams, P. Colegrove, and A. A. Antonysamy, "Microstructure and mechanical properties of wire and arc additive manufactured ti-6al-4v," *Metallurgical and materials transactions A*, vol. 44, no. 2, pp. 968–977, 2013.

[33] Z. Wang, T. A. Palmer, and A. M. Beese, "Effect of processing parameters on microstructure and tensile properties of austenitic stainless steel 304l made by directed energy deposition additive manufacturing," *Acta Materialia*, vol. 110, pp. 226–235, 2016.

[34] F. Bao-Qin, L. Wen-Sheng, Y. Yue, X. Hai-Yan, L. Chun, J. Yu-Zhen, and L. Wei, "Molecular dynamics study of thermal stress and heat propagation in tungsten under thermal shock," *Chinese Physics B*, vol. 22, no. 12, p. 126601, 2013.

[35] R.-H. Xia, X.-G. Tian, and Y.-P. Shen, "Md simulation of a copper rod under thermal shock," *Acta Mechanica Sinica*, vol. 26, no. 4, pp. 599–604, 2010.

[36] Y. Shen, X. Li, X. Sun, Y. Wang, and L. Zuo, "Twinning and martensite in a 304 austenitic stainless steel," *Materials Science and Engineering: A*, vol. 552, pp. 514–522, 2012.

[37] E. Polatidis, W.-N. Hsu, M. Šmíd, T. Panzner, S. Chakrabarty, P. Pant, and H. Van Swygenhoven, "Suppressed martensitic transformation under biaxial loading in low stacking fault energy metastable austenitic steels," *Scripta Materialia*, vol. 147, pp. 27–32, 2018.

[38] E. Polatidis, J. Čapek, A. Arabi-Hashemi, C. Leinenbach, and M. Strobl, "High ductility and transformation-induced-plasticity in metastable stainless steel processed by selective laser melting with low power," *Scripta Materialia*, vol. 176, pp. 53–57, 2020.

[39] J. Venables, "The martensite transformation in stainless steel," *The Philosophical Magazine: A Journal of Theoretical Experimental and Applied Physics*, vol. 7, no. 73, pp. 35–44, 1962.

[40] P. L. Mangonon and G. Thomas, "The martensite phases in 304 stainless steel," *Metallurgical transactions*, vol. 1, no. 6, pp. 1577–1586, 1970.

[41] L. Verlet, "Computer" experiments" on classical fluids. i. thermodynamical properties of lennard-jones molecules," *Physical review*, vol. 159, no. 1, p. 98, 1967.

[42] W. C. Swope, H. C. Andersen, P. H. Berens, and K. R. Wilson, "A computer simulation method for the calculation of equilibrium constants for the formation of physical clusters of molecules: Application to small water clusters," *The Journal of chemical physics*, vol. 76, no. 1, pp. 637–649, 1982.

[43] R. W. Hockney, "The potential calculation and some applications," *Methods Comput. Phys.*, vol. 9, p. 136, 1970.

[44] M. S. Daw and M. I. Baskes, "Embedded-atom method: Derivation and application to impurities, surfaces, and other defects in metals," *Physical Review B*, vol. 29, no. 12, p. 6443, 1984.

[45] J. B. Adams and S. M. Foiles, "Development of an embedded-atom potential for a bcc metal: Vanadium," *Physical Review B*, vol. 41, no. 6, p. 3316, 1990.

[46] R. Watson and L. Bennett, "Transition metals: d-band hybridization, electronegativities and structural stability of intermetallic compounds," *Physical Review B*, vol. 18, no. 12, p. 6439, 1978.

[47] M. Baskes, "Application of the embedded-atom method to covalent materials: a semiempirical potential for silicon," *Physical review letters*, vol. 59, no. 23, p. 2666, 1987.

[48] M. Baskes, J. Nelson, and A. Wright, "Semiempirical modified embedded-atom potentials for silicon and germanium," *Physical Review B*, vol. 40, no. 9, p. 6085, 1989.

[49] M. I. Baskes, "Modified embedded-atom potentials for cubic materials and impurities," *Physical review B*, vol. 46, no. 5, p. 2727, 1992.

[50] P. M. Gullett, A. Slepoy, M. F. Horstemeyer, M. I. Baskes, G. J. Wagner, and M. Li, "Numerical tools for atomistic simulations.," tech. rep., Sandia National Laboratories, 2004.

[51] B.-J. Lee, W.-S. Ko, H.-K. Kim, and E.-H. Kim, "The modified embedded-atom method interatomic potentials and recent progress in atomistic simulations," *Calphad*, vol. 34, no. 4, pp. 510–522, 2010.

[52] B.-J. Lee and M. Baskes, "Second nearest-neighbor modified embedded-atom-method potential," *Physical Review B*, vol. 62, no. 13, p. 8564, 2000.

[53] J.-H. Shim, W.-S. Ko, K.-H. Kim, H.-S. Lee, Y.-S. Lee, J.-Y. Suh, Y. W. Cho, and B.-J. Lee, "Prediction of hydrogen permeability in v–al and v–ni alloys," *Journal of membrane science*, vol. 430, pp. 234–241, 2013.

[54] J. W. Gibbs, *Elementary principles in statistical mechanics*. Courier Corporation, 2014.

[55] M. E. Tuckerman, J. Alejandre, R. López-Rendón, A. L. Jochim, and G. J. Martyna, "A liouville-operator derived measure-preserving integrator for molecular dynamics simulations in the isothermal–isobaric ensemble," *Journal of Physics A: Mathematical and General*, vol. 39, no. 19, p. 5629, 2006.

[56] T. Schneider and E. Stoll, "Molecular-dynamics study of a three-dimensional one-component model for distortive phase transitions," *Physical Review B*, vol. 17, no. 3, p. 1302, 1978.

[57] M. Parrinello and A. Rahman, "Polymorphic transitions in single crystals: A new molecular dynamics method," *Journal of Applied physics*, vol. 52, no. 12, pp. 7182–7190, 1981.

[58] S. Plimpton, "Fast parallel algorithms for short-range molecular dynamics," *Journal of computational physics*, vol. 117, no. 1, pp. 1–19, 1995.

[59] P. Hirel, "Atomsk: A tool for manipulating and converting atomic data files," *Computer Physics Communications*, vol. 197, pp. 212–219, 2015.

[60] A. Stukowski, "Visualization and analysis of atomistic simulation data with ovito–the open visualization tool," *Modelling and Simulation in Materials Science and Engineering*, vol. 18, no. 1, p. 015012, 2009.

[61] R. Hu, Cai, *Fundamentals of Materials Science (Third Edition)*. Shanghai Jiao Tong University Press, 2010.

[62] X. W. Zhou, M. E. Foster, and R. B. Sills, "An fe-ni-cr embedded atom method potential for austenitic and ferritic systems," *Journal of computational chemistry*, vol. 39, no. 29, pp. 2420–2431, 2018.

[63] P. M. Agrawal, B. M. Rice, and D. L. Thompson, "Molecular dynamics study of the effects of voids and pressure in defect-nucleated melting simulations," *The Journal of chemical physics*, vol. 118, no. 21, pp. 9680–9688, 2003.

[64] Y. Zhang and E. J. Maginn, "A comparison of methods for melting point calculation using molecular dynamics simulations," *The Journal of chemical physics*, vol. 136, no. 14, p. 144116, 2012.

[65] S.-N. Luo, T. J. Ahrens, T. Çağın, A. Strachan, W. A. Goddard III, and D. C. Swift, "Maximum superheating and undercooling: Systematics, molecular dynamics simulations, and dynamic experiments," *Physical Review B*, vol. 68, no. 13, p. 134206, 2003.

[66] S.-N. Luo, A. Strachan, and D. C. Swift, "Nonequilibrium melting and crystallization of a model lennard-jones system," *The Journal of chemical physics*, vol. 120, no. 24, pp. 11640–11649, 2004.

[67] S. Alavi and D. L. Thompson, "Simulations of melting of polyatomic solids and nanoparticles," *Molecular Simulation*, vol. 32, no. 12-13, pp. 999–1015, 2006.

[68] A. Ladd and L. Woodcock, "Triple-point coexistence properties of the lennard-jones system," *Chemical Physics Letters*, vol. 51, no. 1, pp. 155–159, 1977.

[69] A. Ladd and L. Woodcock, "Interfacial and co-existence properties of the lennard-jones system at the triple point," *Molecular Physics*, vol. 36, no. 2, pp. 611–619, 1978.

[70] J. N. Cape and L. V. Woodcock, "Molecular dynamics calculation of phase coexistence properties: The soft-sphere melting transition," *Chemical Physics Letters*, vol. 59, no. 2, pp. 271–274, 1978.

[71] J. R. Morris and X. Song, "The melting lines of model systems calculated from coexistence simulations," *The Journal of chemical physics*, vol. 116, no. 21, pp. 9352–9358, 2002.

[72] L.-F. Zhu, J. Janssen, S. Ishibashi, F. Körmann, B. Grabowski, and J. Neugebauer, "A fully automated approach to calculate the melting temperature of elemental crystals," *Computational Materials Science*, vol. 187, p. 110065, 2021.

[73] J. R. Vella, F. H. Stillinger, A. Z. Panagiotopoulos, and P. G. Debenedetti, "A comparison of the predictive capabilities of the embedded-atom method and modified embedded-atom method potentials for lithium," *The Journal of Physical Chemistry B*, vol. 119, no. 29, pp. 8960–8968, 2015.

[74] P. J. Steinhardt, D. R. Nelson, and M. Ronchetti, "Bond-orientational order in liquids and glasses," *Physical Review B*, vol. 28, no. 2, p. 784, 1983.

[75] M. Pascuet and J. R. Fernández, "Atomic interaction of the meam type for the study of intermetallics in the al–u alloy," *Journal of Nuclear Materials*, vol. 467, pp. 229–239, 2015.

[76] Y.-M. Kim, N. J. Kim, and B.-J. Lee, "Atomistic modeling of pure mg and mg–al systems," *Calphad*, vol. 33, no. 4, pp. 650–657, 2009.

[77] B. Jelinek, S. Groh, M. F. Horstemeyer, J. Houze, S.-G. Kim, G. J. Wagner, A. Moitra, and M. I. Baskes, "Modified embedded atom method potential for al, si, mg, cu, and fe alloys," *Physical Review B*, vol. 85, no. 24, p. 245102, 2012.

[78] I. Aslam, M. Baskes, D. Dickel, S. Adibi, B. Li, H. Rhee, M. A. Zaeem, and M. Horstemeyer, "Thermodynamic and kinetic behavior of low-alloy steels: An atomic level study using an fe-mn-si-c modified embedded atom method (meam) potential," *Materialia*, vol. 8, p. 100473, 2019.

[79] M. J. Assael, I. J. Armyra, J. Brillo, S. V. Stankus, J. Wu, and W. A. Wakeham, "Reference data for the density and viscosity of liquid cadmium, cobalt, gallium, indium, mercury, silicon, thallium, and zinc," *Journal of Physical and Chemical Reference Data*, vol. 41, no. 3, p. 033101, 2012.

[80] M. J. Assael, K. Kakosimos, R. M. Banish, J. Brillo, I. Egry, R. Brooks, P. N. Quested, K. C. Mills, A. Nagashima, Y. Sato, *et al.*, "Reference data for the density and viscosity of liquid aluminum and liquid iron," *Journal of physical and chemical reference data*, vol. 35, no. 1, pp. 285–300, 2006.

[81] R. Abdullaev, R. Khairulin, Y. M. Kozlovskii, A. S. Agazhanov, and S. Stankus, "Density of magnesium and magnesium-lithium alloys in solid and liquid states," *Transactions of Nonferrous Metals Society of China*, vol. 29, no. 3, pp. 507–514, 2019.

[82] O. of Standard Reference Materials, "Standard Reference Material 101g 18 Cr-10 Ni Steel (AISI 304L)," standard, National Bureau of Standards, US, Augest 1986.

[83] X. Song, M. Xie, F. Hofmann, T. Illston, T. Connolley, C. Reinhard, R. Atwood, L. Connor, M. Drakopoulos, L. Frampton, *et al.*, "Residual stresses and microstructure in powder bed direct laser deposition (pb dld) samples," *International Journal of Material Forming*, vol. 8, no. 2, pp. 245–254, 2015.

[84] L. E. Kinsler, A. R. Frey, A. B. Coppens, and J. V. Sanders, *Fundamentals of acoustics*. John Wiley & Sons, 1999.

[85] G. Edwards, K. Stiller, G. Dunlop, and M. Couper, "The precipitation sequence in al–mg–si alloys," *Acta materialia*, vol. 46, no. 11, pp. 3893–3904, 1998.

[86] P. H. Ninive, A. Strandlie, S. Gulbrandsen-Dahl, W. Lefebvre, C. D. Marioara, S. J. Andersen, J. Friis, R. Holmestad, and O. M. Lovvik, "Detailed atomistic insight into the $\beta''$ phase in al-mg-si alloys," *Acta Materialia*, vol. 69, pp. 126–134, 2014.

[87] R. Kobayashi, D. Giofré, T. Junge, M. Ceriotti, and W. A. Curtin, "Neural network potential for al-mg-si alloys," *Physical Review Materials*, vol. 1, no. 5, p. 053604, 2017.

[88] Y.-K. Kim, H.-K. Kim, W.-S. Jung, and B.-J. Lee, "Atomistic modeling of the ti–al binary system," *Computational materials science*, vol. 119, pp. 1–8, 2016.

[89] S. B. Maisel, W.-S. Ko, J.-L. Zhang, B. Grabowski, and J. Neugebauer, "Thermomechanical response of niti shape-memory nanoprecipitates in tiv alloys," *Physical Review Materials*, vol. 1, no. 3, p. 033610, 2017.

[90] H.-K. Kim, W.-S. Jung, and B.-J. Lee, "Modified embedded-atom method interatomic potentials for the fe–ti–c and fe–ti–n ternary systems," *Acta Materialia*, vol. 57, no. 11, pp. 3140–3147, 2009.

[91] H.-K. Kim, W.-S. Jung, and B.-J. Lee, "Modified embedded-atom method interatomic potentials for the nb-c, nb-n, fe-nb-c, and fe-nb-n systems," *Journal of Materials Research*, vol. 25, no. 7, pp. 1288–1297, 2010.

[92] Y. Shibuta, S. Sakane, E. Miyoshi, S. Okita, T. Takaki, and M. Ohno, "Heterogeneity in homogeneous nucleation from billion-atom molecular dynamics simulation of solidification of pure metal," *Nature communications*, vol. 8, no. 1, pp. 1–9, 2017.

[93] Y. Fu, J. G. Michopoulos, and J.-H. Song, "Bridging the multi phase-field and molecular dynamics models for the solidification of nano-crystals," *Journal of Computational Science*, vol. 20, pp. 187–197, 2017.